

Wind-driven upwelling and surface nutrient delivery in a semi-enclosed coastal sea

Ben Moore-Maley¹ and Susan E. Allen¹

¹Department of Earth, Ocean and Atmospheric Sciences, University of British Columbia, 2207 Main Mall, Vancouver, BC V6T 1Z4, Canada

Correspondence: Ben Moore-Maley (bmoorema@eoas.ubc.ca)

Abstract.

Wind driven upwelling is an important control on surface nutrients and water properties in stratified lakes and seas. In this study, a high resolution biophysical coupled model is used to investigate upwelling in the Strait of Georgia. The model is forced with surface winds from a high resolution atmospheric forecast and [has been tuned in previous studies to](#) reproduce extensive observations of water level, temperature, salinity, nutrients and chlorophyll with competitive skill relative to similar models of the study region. Five years of hourly surface nitrate and temperature are analyzed in order to characterize the dominant upwelling patterns of the basin. A [prevailing](#) along-axis wind [climatology pattern](#) steered by mountainous topography produces episodic upwelling along the western shore during the spring and fall southeasterlies and along the eastern shore during the summer northwesterlies, as indicated by positive nitrate anomalies. Principal component analysis reveals that these cross-axis upwelling patterns account for nearly one-third of the surface nitrate variance during the productive season. By contrast, nearly half of the surface temperature variance over the same period is dominated by a single, [combined](#) mixing [and diurnal](#) heating-cooling pattern. The principal components associated with these patterns correlate with [along-axis](#) wind stress in a manner consistent with these physical interpretations. The cross-axis upwelling response to wind is similar to other dynamically wide basins where the baroclinic Rossby deformation radius is smaller than the basin width. However, the nitrate anomaly during upwelling along the eastern shore is stronger in the northern basin, which may be indicative of an along-axis pycnocline tilt or an effect of the background along-axis stratification gradient due to the Fraser River. Our findings highlight an important spatio-temporal consideration for future ecosystem monitoring.

1 Introduction

Wind driven upwelling is ubiquitous in the coastal ocean (Kämpf and Chapman, 2016) and in large, enclosed seas (e.g., Silvestrova et al., 2019; Lehmann et al., 2012; Plattner et al., 2006). This process provides an important pathway for vertical nutrient transport into the euphotic zone (Messié and Chavez, 2015) but can also be a source of environmental stress by introducing large amplitude fluctuations of temperature, dissolved oxygen, pCO₂, pH and aragonite saturation state near the coast (Chan et al., 2017). Consequently, upwelling variability can dramatically alter seasonal biological community structure across a wide trophic range (Barth et al., 2007), and persistent upwelling is often a defining feature of ecosystems such as along

25 Pacific and Atlantic eastern boundaries (Chavez and Messié, 2009). Additionally, upwelling has been observed to influence phytoplankton distributions in large lakes (Mziray et al., 2018; Bouffard et al., 2018) and can mitigate or exacerbate problems associated with anthropogenic eutrophication in urbanized regions such as cyanobacteria blooms in the Baltic Sea (Wasmund et al., 2012) and hypoxia in Lake Erie (Rowe et al., 2019).

30 In enclosed basins, coastal upwelling describes the pycnocline displacements that result from wind driven horizontal divergence near a coastline and any oscillations that follow (Csanady, 1977; Shintani et al., 2010). However, the structure of these pycnocline displacements strongly depends on the dynamic width of the basin scale (Cushman-Roisin et al., 1994). This scale dynamic width can be described by the physical width of the basin relative to the internal Rossby deformation radius L_R which is defined in a two-layer approximation as

$$L_R = \frac{NH}{f} \quad (1)$$

35 where N is the Brunt-Väisälä frequency, H is the water depth and f is the Coriolis parameter g is the gravitational acceleration, $\Delta\rho$ is the density difference across the pycnocline, ρ_0 is the background density and h_1 and h_2 are the respective upper and lower layer thicknesses. Given a sustained, along-axis wind impulse, if the basin is much wider than L_R then Ekman fluxes freely develop and the pycnocline displacement is cross-axis. If the basin is narrower than L_R then Ekman fluxes are rapidly opposed by cross-axis pressure gradients and cannot fully form, forcing the surface layer transport to flow along-axis which sets up an end-to-end pycnocline tilt (Csanady, 1982). Upwelling studies across a range of dynamic scales widths support this theory. Cross-axis upwelling is primarily observed in large seas like the Baltic Sea sub-basins (Bednorz et al., 2019; Delpeche-Ellmann et al., 2017; Zhurbas et al., 2008) and the North American Great Lakes (Plattner et al., 2006; Csanady, 1977) while along-axis upwelling is primarily observed in narrow basins like the glacial reservoirs of British Columbia (Imam et al., 2013; Laval et al., 2008). The along-axis pycnocline setup in lakes progresses as a set of internal seiche modes excited by the initial wind impulse (Stevens and Lawrence, 1997; Stevens and Imberger, 1996). If the lake is wide enough, these seiches can be amphidromic to the point of resembling Kelvin waves, even if the initial pycnocline setup is along-axis (Roberts et al., 2021; Bouffard and Lemmin, 2013; Valerio et al., 2012).

45 Upwelling can be influenced by several factors in addition to dynamic scale. For example, local wind variability may produce secondary upwelling features superimposed on the basin scale setup. Wind stress curl has been implicated in observations of cyclonic circulation cells and open water upwelling in large lakes such as Lake Baikal (Troitskaya et al., 2015) and Lake Michigan (Schwab and Beletsky, 2003), while wind is aligned primarily along axis in narrow mountain lakes due to topographic steering (e.g., Quesnel Lake, Thompson et al., 2020). This along-axis tendency is particular strong in high-latitude fjords where katabatic winds are common (Lundesgaard et al., 2019; Spall et al., 2017). Topographic features such as thalweg geometry in narrow lakes (Shintani et al., 2010) and offshore bottom slope in wide basins (Delpeche-Ellmann et al., 2018; Choboter et al., 2011; Lentz and Chapman, 2004) can affect the strength of upwelling at the coast. In wide basins and along continental margins, the along-shore current that forms during cross-shore upwelling can separate from the coast over shallow banks to conserve potential vorticity, as observed in the Baltic Sea (Gurova et al., 2013) and along the central Oregon coast (Castelao and Barth, 2005). If spatial salinity gradients are strong, near river plumes for example, baroclinic pressure gradients

can weaken or amplify the wind-driven pycnocline tilt (Li and Li, 2012). Finally, bottom roughness and turbulent bottlenecks can result in complete damping of the internal wave response in narrow lakes (e.g., Nechako Reservoir, Imam et al., 2013).

In this study, we explore wind driven upwelling in the Salish Sea estuarine fjord network on the Canadian west coast. We focus our analysis on the Strait of Georgia (SoG), which is the largest and most protected basin in the Salish Sea. The SoG is a globally significant ecosystem that provides critical habitat to several keystone fisheries including the iconic Fraser River sockeye salmon (Thomson et al., 2012) and the endangered Southern Resident Killer Whale (Wasser et al., 2017). The SoG also contains over half of the shellfish aquaculture leases in Pacific Canada, most of which are concentrated in just two sheltered regions. Salinity gradients in the SoG are large due to significant runoff from surrounding mountainous watersheds and deep estuarine inflows from the Pacific Ocean. These oceanic inflows combined with local remineralization of organic matter make the deep SoG nutrient and carbon rich (Sutton et al., 2013; Ianson et al., 2016) and transiently hypoxic (Johannessen et al., 2014), while the surface is nutrient and carbon poor due to strong seasonal primary productivity. Several recent studies have sought to link changes in this productivity to the significant declines in returning salmon in recent years. While no long term changes have been identified (Johannessen et al., 2021), interannual variability in spring bloom timing has been implicated as a possible factor (Thomson et al., 2012).

The importance of wind in controlling this productivity is well-established. During the transition from winter to spring, the expansion of the North Pacific High suppresses winter storm activity in the region (Bakri and Jackson, 2019). Calm winds and clear skies provide light and stratification for a spring phytoplankton bloom to occur (Collins et al., 2009). Surface nutrients are rapidly depleted and remain low throughout the summer, with small phytoplankton persisting through the nutrient depleted conditions (Del Bel Belluz et al., 2021; Haigh and Taylor, 1991). Further wind activity throughout this period introduces additional nutrients to the surface allowing smaller blooms to occur (Del Bel Belluz et al., 2021). Additionally, large surface pCO₂ fluctuations have been observed to occur near sensitive shellfish aquaculture zones in the northern SoG following northerly wind impulses (Evans et al., 2018). Poor spatial and temporal resolution in most existing studies has prevented a more detailed analysis of surface nutrient delivery in the SoG, and so these nutrient and pCO₂ pulses are generally attributed to vertical wind mixing (e.g., Del Bel Belluz et al., 2021; Yin et al., 1997). However, cross-axis asymmetry of satellite sea surface temperature (Evans et al., 2018) and modelled surface nitrate (Olson et al., 2020) identified during more recent along-axis wind events in the northern SoG suggests that upwelling is a significant driver of these nutrient pulses.

Here we analyze 5 years of hourly, high resolution surface nitrate and temperature results from a biophysical coupled model of the Salish Sea along with hourly, high resolution surface wind forcing fields from an operational Canadian weather model in order to better characterize the mechanism of wind driven surface nutrient delivery in the SoG. Using principal component analysis, we identify dominant leading modes of variability that account for significant fractions of the total variance of each tracer following the spring bloom. By examining the persistent spatial patterns and power spectra of the surface nitrate and temperature anomalies that correlate with modes, and the spectral coherence and correlation between these tracer modes and the wind forcing record, we attribute the variance from each mode to a set of then characterize the physical processes including upwelling mechanisms that determine each spatial pattern according to the sign of the correlation to wind stress. This study is the first to explicitly identify quantify the contribution of wind driven upwelling to the variability of surface nitrate in the SoG,

and the results ~~introduce~~ ~~highlight~~ a fundamental nutrient delivery mechanism that is currently unexplored in SoG ecosystem studies. This study also provides a further basis for interpreting surface temperature and pCO₂ fluctuations like those observed in the northern SoG (Evans et al., 2018). Finally, this study corroborates the well-established cross-axis patterns of upwelling in ~~large~~ ~~dynamically wide~~ basins such as the Baltic Sea and North American Great Lakes but for a strongly stratified estuarine fjord system.

2 Methods

100 2.1 Study area

The SoG is approximately 200 km long, 40 km wide and 400 m deep along the thalweg (Fig. 1). The primary connection to the Pacific Ocean is located at the southern end of the basin through Haro and Rosario Straits while a secondary connection to the north through Johnstone Strait accounts for a small fraction of the oceanic exchange (Pawlowicz et al., 2007). The exchange between the SoG and the Pacific Ocean is forced by estuarine circulation (MacCready et al., 2021) fed by local watersheds as well as the approximately 220,000 km² Fraser River drainage basin. This circulation cell is significantly modulated by mixing due to 2-4 m amplitude mixed diurnal-semidiurnal tides (Foreman et al., 1995), primarily over the respective 100 and 50 m sill depths in the narrow Haro and Johnstone Straits. This tidal modulation recycles outgoing brackish water back into the intermediate and deep SoG – the incoming water through Haro Strait, for example, is composed of approximately 60% outgoing surface water (Pawlowicz et al., 2019). However, annual flushing maintains high salinity in the deep basin (Masson, 110 2002) and strong vertical salinity gradients ~~below the brackish surface layer~~ ~~during peak runoff~~.

Oceanic inflows driven by estuarine circulation are the primary sources of nitrate (Mackas and Harrison, 1997) and dissolved inorganic carbon (Ianson et al., 2016) to the SoG. ~~Local remineralization combined with long residence times amplify these tracers in the deep SoG and reduce deep dissolved oxygen to increasingly hypoxic levels (Johannessen et al., 2014; Ianson et al., 2016). Seasonal cycles of wind, solar and freshwater forcing determine the nitrate and pCO₂ levels in the surface. During the spring expansion of the North Pacific High, storm suppression facilitates the spring phytoplankton bloom (Collins et al., 2009) which depletes surface nitrate and increases surface pCO₂ (Moore-Maley et al., 2016). These surface conditions persist throughout the summer, enhanced by the combined stratifying effects of solar irradiance and river runoff (Masson and Peña, 2009). The latter reaches a maximum in early summer during the Fraser River freshet and has the strongest influence in the southern SoG near the Fraser River delta (Pawlowicz et al., 2017). Strong summer wind events have been shown to briefly replenish surface nutrients (Del Bel Belluz et al., 2021) and decrease surface pCO₂ (Evans et al., 2018) against this background stratification. Surface nitrate is not fully depleted at the ends of the SoG near Haro and Johnstone Straits due to tidal mixing (Masson and Peña, 2009; Olson et al., 2020). The strength of this mixing varies over a fortnightly tropical tidal cycle (Thomson et al., 2020).~~

120

~~Additionally, these tracers are constantly recirculated into the SoG via tidal mixing. This process proceeds differently at opposite ends of the basin. At the southern end, the recirculated tidal jet from Haro Strait readily subducts into the intermediate layer as a gravity current (Thomson et al., 2020) and transiently reaches the surface through slow upward mixing followed by~~

125

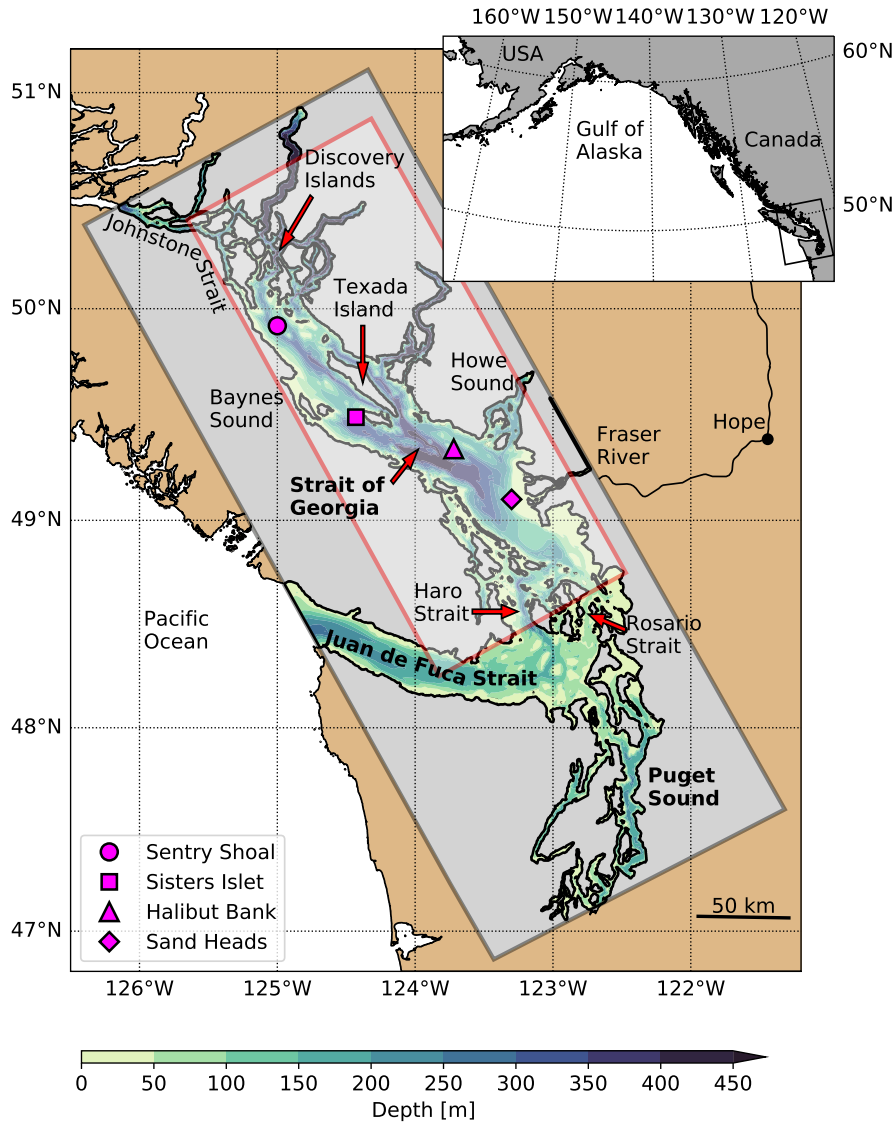


Figure 1. Map of the Salish Sea study region with the SalishSeaCast model domain overlaid as a gray box and contoured bathymetry. Relevant geographic features, meteorological observing platforms (magenta symbols) and ~~modelled surface nitrate locations (stars)~~ the subdomain used for principal component analysis (red box) referenced in this study are also shown. ~~The Texada and Central Vancouver Island (VI) locations are positioned along the respective eastern and western shores of the Strait of Georgia where upwelling dominates, while the Discovery Passage and Boundary Pass locations are positioned at the northern and southern ends of the basin where tidal mixing dominates.~~ Coastline data were obtained from the GSHHS database (Wessel and Smith, 1996).

~~entrainment and frontal dynamics surrounding the Fraser River plume (Parsons et al., 1981). At the northern end of the basin,~~

the recirculated tidal jet is injected directly into the surface layer from Johnstone Strait at near-neutral buoyancy and flows south along the western side of the basin while gradually sinking toward Baynes Sound (Olson et al., 2020).

130 Away from these tidal nutrient sources, stratification and river plume dynamics determine the overall chlorophyll biomass distribution in the SoG. Stratification reaches a maximum in the Fraser plume at the southern end of the basin and gradually decreases toward the north (Masson and Pena, 2009). During the productive season, the chlorophyll distribution reflects the stratification gradient in two important ways. While surface chlorophyll generally decreases from south to north following the stratification gradient (Suchy et al., 2019; Masson and Pena, 2009), the chlorophyll depth range increases from south
135 to north (Masson and Pena, 2009) such that total integrated chlorophyll shows no consistent bias toward any one region (Pawlowicz et al., 2020). An exception to this pattern is found directly within the Fraser plume where phytoplankton are restricted to a thin surface layer (Halverson and Pawlowicz, 2013) and river turbidity reduces light availability (Moore-Maley et al., 2016), although the plume boundary can produce elevated chlorophyll due to frontal dynamics (Parsons et al., 1981). A subtle, cross-axis stratification gradient also arises due the disproportionate summer runoff from the glacially fed watersheds
140 along the eastern side of the basin. This gradient is consistent with modelled (Pena et al., 2016) and observed (Suchy et al., 2019) cross-axis chlorophyll gradients and has been implicated as a driver of observed flagellate community clusters along the northeastern coastline (Haigh and Taylor, 1991).

Wind and cloud fraction are important drivers of seasonal chlorophyll cycles. As mentioned earlier, wind relaxation and weakening cloud cover facilitate the spring diatom bloom (Collins et al., 2009) and subsequent wind activity enhances chlorophyll
145 by bringing nutrients to the surface (Yin et al., 1997). Local weather

Wind over the SoG is determined by the synoptic scale meteorology of the northeast Pacific Ocean. Consistent groupings of three dominant synoptic types have resulted from cluster analyses of meteorological data at marine (Bakri and Jackson, 2019) and land-based (Stahl et al., 2006) observing platforms in BC. These types can be summarized as (1) a summer type with a pronounced North Pacific High and northwesterly, along-isobar wind at the coast, (2) a winter type with a pronounced Aleutian
150 Low and strong southeasterly, cross-isobar wind at the coast and (3) a transition type between the two pressure centers that dominates during the shoulder seasons (Bakri and Jackson, 2019; Stahl et al., 2006). The strongest observed winds at marine locations are associated almost exclusively with the winter synoptic types, and spatial variability between locations is consistent with the presence of extra-tropical cyclones (Bakri and Jackson, 2019). Conversely, summer synoptic types are weaker but more persistent than winter types in terms of their recurrence probability, and they are also generally longer lived with a maximum
155 duration of 15-20 days relative to the shorter 5-10 day maximum of the winter types (Stahl et al., 2006). Winter storm activity is dominated by extra-tropical cyclones that form along the polar jet stream and produce primarily southeast winds and significant precipitation when they make landfall along the outer coast (Read, 2015; Thompson et al., 2020). As the North Pacific High expands during the transition between winter and summer, these storms are suppressed and the local wind follows the prevailing wind patterns which are northwest (Bakri and Jackson, 2019; Stahl et al., 2006). The dominant northwesterly and southeasterly
160 directions align closely with the primary axis of the SoG, and further topographic steering constrains the local wind to blow primarily along-axis (Bakri et al., 2017a). A significant exception to this climatology are the winter gap winds that occur in the Fraser River Valley and Howe Sound (Bakri et al., 2017b; Jackson, 1996; Overland and Walter Jr., 1981).

2.2 Numerical simulations

The SalishSeaCast model employed in this study is a quasi-operational, biophysical-coupled, Salish Sea configuration of the Nucleus for European Modelling of the Ocean (NEMO) 3.6 engine, developed and maintained by the UBC Mesoscale Ocean and Atmospheric Dynamics (MOAD) Laboratory (Olson et al., 2020; Soontiens and Allen, 2017; Soontiens et al., 2016). NEMO is a finite difference, curvilinear, hydrostatic, primitive equation ocean model with extensive functionality for coupling additional system components such as biogeochemistry, passive tracers, Lagrangian particles and sea ice (Madec et al., 2017). The SalishSeaCast domain has approximately 500 m horizontal resolution and 40 z -coordinate layers approximately 1 m thick near the surface, coarsening to 27 m in the bottom layer ~~with partial steps at the bottom boundary~~. The model uses split-explicit time stepping with barotropic and baroclinic time steps of 2 s and 40 s, respectively. A 2 s vertical time step is also specified to maintain stability in the tidal mixing regions where vertical velocities are large. Lateral mixing is constrained by constant horizontal eddy viscosity and diffusivity values of $1.5 \text{ m}^2 \text{ s}^{-1}$, and vertical mixing is parameterized using a k - ϵ turbulence closure scheme with background vertical eddy viscosity and diffusivity values of $1 \times 10^{-6} \text{ m}^2 \text{ s}^{-1}$. Partial slip conditions are imposed at lateral closed boundaries, and quadratic bottom friction and a log layer parameterization are imposed at the bottom boundary.

The SalishSeaCast ecosystem model, SMELT (Salish Sea Model Ecosystem-Lower Trophic), is a nutrient-phytoplankton-zooplankton-detritus (NPZD) scheme coupled to the physics engine using the NEMO Tracers in the Ocean Paradigm (TOP) module (Olson et al., 2020). SMELT simulates the dominant functional groups of the Salish Sea, specifically: 3 nutrient classes (nitrate, ammonium, silica), 3 phytoplankton classes (diatoms, small flagellates, *Mesodinium rubrum*), 2 grazer classes (microzooplankton, mesozooplankton) and 3 detrital pools (biogenic silica, particulate organic nitrogen, dissolved organic nitrogen). *M. rubrum* is a mixotrophic ciliate that can contribute significantly to observed phytoplankton biomass in the Salish Sea (Hansen et al., 2013), and both the autotrophic and heterotrophic behaviors attributed to this ciliate are simulated in the model. While an early diatom-only version of SMELT was used to predict the spring bloom timing in the SoG (Collins et al., 2009), the multiple NPZD classes represented in the present version are necessary to accurately resolve the post-bloom dynamics that govern surface nitrate concentration (Olson et al., 2020).

Open boundaries in Juan de Fuca Strait and Johnstone Strait are forced with eight tidal constituents (K1, O1, P1, Q1, M2, K2, N2, S2) determined according to Foreman et al. (2000) and Thomson and Huggett (1980), respectively. Surface height is additionally forced at the Juan de Fuca boundary using a storm surge forecast at Neah Bay, USA provided by the US National Oceanic and Atmospheric Administration (NOAA). The Flather radiation condition (Flather, 1994) is used for barotropic tidal velocities and sea surface height, a modified Orlanski radiation condition (Marchesiello et al., 2001) with a sponge layer is used for baroclinic velocities, and the Flow Relaxation Scheme (Madec et al., 2017) is used for temperature and salinity within 10 grid points from the boundary. Temperature, salinity and nitrate at the Juan de Fuca open boundary are obtained from detided outputs of the University of Washington LiveOcean model (Fatland et al., 2016). Dissolved silica is further estimated from LiveOcean nitrate (Olson et al., 2020). Temperature, salinity, nitrate and silica at the Johnstone Strait boundary are set based on

monthly climatologies provided by the Hakai Institute. Ammonium at both boundaries is set to a mean observed profile (Olson et al., 2020).

Surface momentum, heat, precipitation, and sea level pressure are forced with results from the High Resolution Deterministic Prediction System (HRDPS), which is a 2.5 km operational Pan-Canadian weather forecast model developed and maintained
 200 by Environment and Climate Change Canada (ECCC) (Milbrandt et al., 2016). Wind stress $\vec{\tau}$ is calculated according to a quadratic wind speed parameterization

$$\vec{\tau} = \rho_a C_s U \mathbf{U} \quad (2)$$

where \mathbf{U} is the surface wind velocity vector, U is the surface wind speed, ρ_a is the surface air density and C_s is the surface drag coefficient calculated according to Hellerman and Rosenstein (1983). The wind stress boundary condition is applied to
 205 the surface momentum via the vertical momentum flux equation

$$\frac{\vec{\tau}}{\rho_0} = A_v \frac{\partial \mathbf{u}_h}{\partial z} \Big|_{z=1} \quad (3)$$

where \mathbf{u}_h is the horizontal fluid velocity vector, A_v is the vertical eddy diffusivity determined by the k - ϵ parameterization, ρ_0 is the background density and z is the vertical coordinate.

Monthly climatologies are used to prescribe runoff from the approximately 150 rivers included in the model domain (Mor-
 210 rison et al., 2012). Upper Fraser River runoff is prescribed separately using daily observations provided by ECCC from a flow gauge approximately 150 km upstream at Hope, BC while the lower Fraser tributaries are included in the climatologies. Temperature in all rivers is set according to a monthly climatology of Fraser River temperature based on ECCC observations at Hope (Allen and Wolfe, 2013), and river salinity is set to zero. Biological river tracers are determined according to ECCC and UBC observations in selected watersheds including the lower Fraser (Olson et al., 2020). For example, Fraser River nitrate is
 215 set to a seasonal cycle that varies between 8.37 $\mu\text{M N}$ during the winter and 2.88 $\mu\text{M N}$ during the freshet.

The tidal constituents at the open boundaries have been tuned to improve model skill at 31 tidal gauges located throughout the model domain (Soontiens et al., 2016). This tuning exercise prioritized high skill in the SoG region, and the tidal predictions outside of the SoG are thus less accurate. However, tidal mixing between Juan de Fuca Strait and the SoG is sufficiently accurate to resolve deep basin flushing, which is important for controlling temperature and salinity in the SoG over time
 220 (Soontiens and Allen, 2017). Soontiens and Allen (2017) further determined that the largest improvements to deep flushing were achieved by removing a numerical kinetic energy sink artifact known as the Hollingsworth instability (Hollingsworth et al., 1983). Temperature, salinity and the biological tracers have been rigorously evaluated against observations from several comprehensive, multi-year sampling programs covering the full model domain (Olson et al., 2020). Temperature is the most accurately predicted tracer with no significant bias. Salinity is predicted nearly as accurately as temperature except at low
 225 salinity, especially near the coast where the limitations of the monthly watershed climatology become important and coastal processes like wetting and drying are unresolved in the model. Model nitrate, dissolved silica and chlorophyll all demonstrate average to strong skill relative to similar models of the study region (e.g., Khangaonkar et al., 2018), with nitrate performing the strongest of the three tracers. Surface nitrate in the SoG is biased low by approximately 1-2 μM during the productive

season since model phytoplankton are slightly more effective at depleting surface nutrients than observed communities. This
230 ~~phenomenon is common~~ problem has also been encountered in previous biological modelling studies of the SoG (e. g., Moore-
Maley et al., 2016).

A 5-year hourly hindcast record of the SalishSeaCast model was obtained by performing parallel CPU runs on a high
performance computing platform. A restart file was produced by initializing the model tracers according to several data sets
(Olson et al., 2020) and spinning up from rest over ~~a one~~ two consecutive years of 2013 forcing data period (Olson et al., 2020).
235 This restart file was then used to initialize the hindcast at the beginning of 2013 and run through the end of 2019. We limit our
analysis to years 2015-2019 during the ~~productive season~~ period between spring and fall when the surface nitrate is depleted.
We define these seasonal bounds using a nitrate threshold of $2 \mu\text{M}$ applied to the spatial ~~averaged median of the~~ surface nitrate
concentration over an open water region of the SoG to be described in Section 3 ~~sub-region~~. Specifically, the analysis window
begins 5 days after the surface nitrate first drops below the threshold value and ends 5 days before the surface nitrate last rises
240 above the threshold value. The 5-day buffer is included to further eliminate the biological influence of large blooms on the
upwelling signal. We refer to this period as the “productive season”.

2.3 Data methods

Principal component analysis

We perform principal component analysis (PCA) as described by Preisendorfer (1988) on the hourly surface nitrate and tem-
245 perature records during the productive season, and we exclude Juan de Fuca Strait and Puget Sound to remove the variance
contributed by processes outside of the SoG ~~seasonal windows defined by the $2 \mu\text{M}$ nitrate threshold. We only consider the~~
~~region including the SoG and the tidal mixing areas~~ (Fig. 1, red box). and To prepare the fields for PCA, we resample the model
grid to a resolution of 2.5 km in order to improve computation time and then “de-trend” the resampled nitrate and temperature
records ~~are “de-trended”~~ by subtracting a low-pass filtered signal ~~This signal is obtained using a finite impulse response (FIR)~~
250 ~~filter with a 1235 h, or approximately 50 d, Blackman window. The 1235 h Blackman window attenuates the signal 10-fold at~~
~~an effective 841 h or with an~~ approximately 35 d cutoff frequency. ~~which The 35 d cutoff was chosen is sufficient~~ to remove
any seasonal ~~scale climatological~~ variability ~~but long enough to~~ still present during the productive season while retaining the
~~effects of low~~ processes occurring in the subtidal frequency range such as the fortnightly tidal ~~variations~~ cycle and the synoptic
scale wind events introduced in Section 2.1. A finite impulse response (FIR) filter with a 1235 h Blackman window is used,
255 which attenuates the signal 10-fold at an effective 841 h, or 35 d, cutoff frequency.

~~The sub-sampled spatial grid points~~ To perform the PCA matrix operations, the spatial dimensions of each tracer record are
treated as a set of p independent variables over a time series of length n such that ~~each tracer record is the filtered nitrate and~~
temperature arrays are each reshaped to an $n \times p$ matrix \mathbf{Z} . The principal component (PC) loadings and empirical orthogonal
functions (EOF) are obtained using the singular value decomposition of \mathbf{Z}

$$260 \quad \mathbf{Z} = \mathbf{A}'\mathbf{L}^{1/2}\mathbf{E}^T = \mathbf{A}\mathbf{E}^T \quad (4)$$

where \mathbf{A} is the $n \times p$ PC loadings matrix, \mathbf{L} is the $p \times p$ triangular eigenvalue matrix and \mathbf{E} is the $p \times p$ EOF pattern matrix (Preisendorfer, 1988).

The orthogonality constraint of PCA can limit the extent to which each mode of variability actually captures the full pattern of a given physical phenomenon (Westra et al., 2010). We thus introduce a $p \times p$ rotation matrix \mathbf{R} such that

$$265 \quad \mathbf{Z} = \mathbf{A}(\mathbf{R}\mathbf{R}^T)\mathbf{E}^T = (\mathbf{A}\mathbf{R})(\mathbf{E}\mathbf{R})^T = \mathbf{B}\mathbf{U}^T \quad (5)$$

where \mathbf{B} is the rotated $n \times p$ PC loading matrix and \mathbf{U} is the rotated $p \times p$ EOF pattern matrix. \mathbf{R} is chosen such that the varimax criterion

$$f(\mathbf{R}) = \sum_{j=1}^p \left\{ \frac{1}{n} \sum_{t=1}^n [b_j^2(t)]^2 - \left[\frac{1}{n} \sum_{t=1}^n b_j^2(t) \right]^2 \right\} \quad (6)$$

is maximized (Kaiser, 1957), where $b_j(t)$ are the elements of \mathbf{B} (Preisendorfer, 1988, ch. 7d). We use the Simultaneous Factor
270 Varimax Solution algorithm described by Horst (1965, ch. 18.4) in order to find \mathbf{R} .

Spectral analysis and correlation

We define a reference, along-axis HRDPS wind stress record by rotating the meridional wind velocity 55.6° CCW, computing the wind stress according to Equation 2 and taking the spatial median over an open water region of the SoG to be described in Section 3. We determine the power spectral density (PSD) for the PC loadings time series of a given mode and the spectral
275 coherence between each mode and our reference, along-axis wind stress using the multitaper ensemble method (Percival and Walden, 1993). For PSD, we use a normalized half-bandwidth of 2.5 or an approximate dimensional smoothing bandwidth of 0.007 d^{-1} , which is sufficiently narrow to resolve any fortnightly and monthly subtidal peaks that may be present. For spectral coherence, we increase this half-bandwidth to 15 or an approximate dimensional bandwidth of 0.043 d^{-1} since we are more interested in broadly-distributed subtidal wind forcing. The maximum effective ensemble size is twice the half-bandwidth, or 5
280 tapers for the PSD calculation and 30 tapers for the coherence calculation. We define the significance threshold for coherence as the 99th percentile of the coherence between two white noise signals.

We use a Bayesian Markov Chain Monte Carlo (MCMC) method to determine the linear regression and correlation between each PC mode and the along-axis HRDPS wind stress (see Section 2.4 below). The method uses a No-U-Turn Sampler (NUTS) with a sample size of $n = 1000$. The NUTS sampler returns normal distributions of the linear regression slope and intercept.
285 Confidence intervals are then determined by drawing 1000 samples from these distributions, and we consider the correlation significant if the 99% confidence intervals do not include a zero slope. We define a Bayesian correlation coefficient in terms of the variances of the fit parameters

$$R^2 = \frac{\text{var}(y_{\text{predicted}})}{\text{var}(y_{\text{predicted}}) + \text{var}(y_{\text{residual}})} \quad (7)$$

where $\text{var}(y_{\text{predicted}})$ is the variance of the set of predicted values by the linear regression model and $\text{var}(y_{\text{residual}})$ is the
290 variance of the set of residuals. We expect that wind-driven processes such as upwelling and mixing depend on cumulative

rather than instantaneous wind stress. We thus perform a running back-average on the reference HRDPS wind stress record over the minimum averaging window required to maximize R^2 .

PCA mode attribution

We assign the dominant physical phenomena that can drive changes in surface nitrate and temperature during the productive season and at frequencies higher than the 35 d high-pass filter cutoff into the following four categories: wind-driven upwelling, wind-driven mixing, fortnightly modulation of tidal mixing and diurnal heating and cooling. While biological nitrate drawdown is the primary surface nitrate sink, drawdown events are tightly coupled to wind events and we thus interpret the underlying process to be wind-driven. We also disregard changes in freshwater input since low summer precipitation keeps runoff steady in the subtidal frequency range and variability in the position of river plumes is primarily stochastic or driven by wind and tides.

We use the following four criteria for attributing specific surface nitrate and temperature PCA modes to these physical phenomena:

1. **Spatial anomalies** The EOF spatial pattern matches the expected surface tracer anomalies from a given process. Specifically, wind-driven upwelling produces coastal anomalies along the sides of the basin, tidal mixing modulation produces anomalies in the tidal mixing regions, and wind-driven mixing and diurnal heating and cooling all produce uniform anomalies in the stratified areas of the basin.
2. **Power spectra** The power spectral density (PSD) of the PC loadings contains the expected features of the given process. Specifically, wind-driven upwelling and mixing both produce broadly distributed energy throughout the subtidal frequency range, tidal mixing produces concentrated energy peaks in the fortnightly and monthly subtidal bands, and diurnal heating and cooling produces concentrated energy at the daily frequency.
3. **Wind coherence** The significance and frequency bands of the coherence between the PC loadings and the along-axis wind stress match the expected wind dependence associated with the given process. Specifically, wind-driven upwelling and mixing demonstrate significant coherence in the subtidal frequency range. Coherence is not significant for tidal mixing or diurnal heating and cooling.
4. **Wind correlation** The correlation between the PC loadings and the along-axis wind stress matches the expected wind dependence associated with the given process. Specifically, PCA modes attributed to wind mixing are correlated symmetrically with both positive and negative along-axis wind stress while PCA modes attributed to wind-driven upwelling are correlated asymmetrically with only one direction of wind stress. Correlation is insignificant for tidal mixing and diurnal heating and cooling.

320 2.4 Analysis software and Visualization

SalishSeaCast results and HRDPS forcing data were stored and accessed in the Network Common Data Form (NetCDF) format (Unidata, 2019). All analysis and visualization was performed using Python 3.9 and the Jupyter development environment (Kluyver et al., 2016). In addition to the Python standard library, the following packages were used: Xarray for NetCDF processing (Hoyer and Hamman, 2017), NumPy for arrays and matrix operations (Harris et al., 2020), SciPy for filtering and spectral analysis (Harris et al., 2020) (Virtanen et al., 2020), PyMC3 for Bayesian MCMC linear regression (Salvatier et al., 2016), Pandas for loading and processing observed wind data (McKinney, 2010), Matplotlib for plotting (Hunter, 2007), Cartopy for map projections (Met Office, 2010-2015) and Windrose for polar histograms (Roubeyrie and Celles, 2018).

3 Results

3.1 Overview of 5 year record and comparisons with observations

330 In order to illustrate how SalishSeaCast resolves upwelling in the SoG, we first compare snapshots of hindcast surface temperature and nitrate with surface temperature observations from the Moderate Resolution Imaging Spectroradiometer (MODIS) instrument aboard the NASA Aqua satellite. We selected four cloud-free images that overlap with sustained, along-axis wind events during the hindcast period. Two of these images were taken during southeast wind (4 September 2015 and 12 September 2018) and two were taken during northwest wind (30 July 2016 and 20 June 2019). In all four images, a cross-axis temperature gradient toward the right of the wind direction is clearly visible in the MODIS surface temperature observations (Fig. 2, top row), and the dominant spatial features of these gradients are reproduced in the SalishSeaCast surface temperature fields (Fig. 2, middle row). These features include a cold coastal upwelling band to the left of the wind direction, offshore and downwind advection of the upwelling plume, and along-axis variability. The cold upwelling regions of the surface temperature fields also overlap with positive nitrate anomalies in the SalishSeaCast surface nitrate fields (Fig. 2, bottom row). From these 340 four snapshots, upwelling appears to be consistently strong in specific areas and weak or patchy in others. Along the eastern shore, upwelling is strongest in the northern and central SoG and the northern tip of Texada Island, and weakens significantly in the southern SoG near the Fraser River mouth. Along the western shore, upwelling is most prominent in the northern SoG near Baynes Sound. In addition, large nitrate plumes appear to be advected northward from the Gulf Islands Haro Strait region where tidal mixing is strong.

345 We next compare the 5 year HRDPS hourly surface wind velocity record with 5 years of hourly wind velocity observations at the four open water, meteorological observing stations shown in Fig. 1 (magenta symbols). Sand Heads and Sisters Islet are navigational light stations equipped with meteorological sensors maintained by ECCC, while Halibut Bank and Sentry Shoal are 3 m discus buoys maintained by the Department of Fisheries and Oceans Canada (DFO). At all four stations, an along-axis wind climatology dominance is clear from the observed wind velocity record in winter (Fig. 3, top row) and summer (Fig. 3, second row from bottom), and the primary features of this record are reproduced by the HRDPS wind velocities (Fig. 3, second row from top and bottom row). In addition to along-axis dominance, these features include a seasonal separation between strong

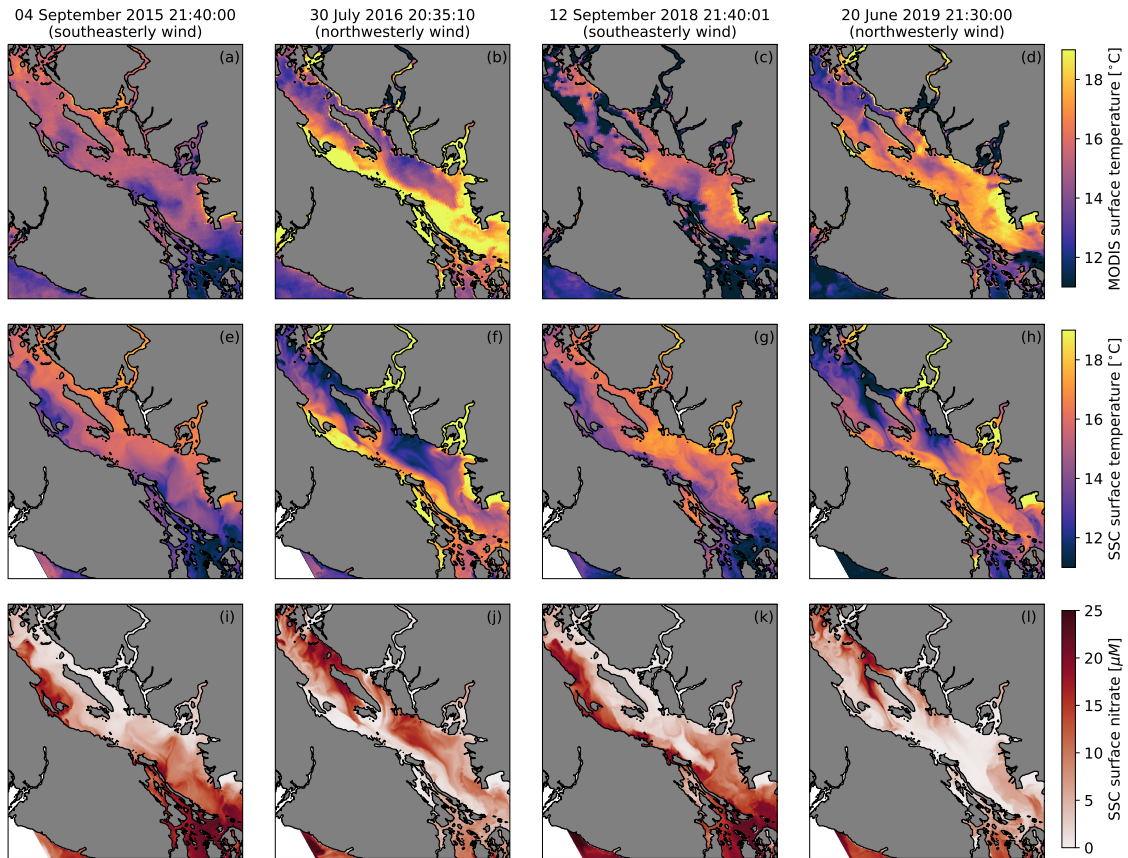


Figure 2. Surface temperature observations from the Moderate Resolution Imaging Spectroradiometer (MODIS) instrument aboard the NASA Aqua satellite (a-d), SalishSeaCast (SSC) surface temperature (e-h) and SSC surface nitrate (i-l) during four cloud-free upwelling events. All times are in UTC. The surface fields shown on 4 September 2015 and 12 September 2018 occurred during southeasterly wind and show cold, nitrate-rich upwelling along the Vancouver Island coast, while the surface fields shown on 30 July 2016 and 20 June 2019 occurred during northwesterly wind and show upwelling along the opposing BC mainland coast and the western side of Texada Island. The SSC fields reproduce the overall spatial structure observed in the MODIS images.

southeasterly winter wind and weaker northwesterly summer wind. ~~There is also a tendency for stronger~~ Winter southeasterly winds are stronger in the northern SoG relative to the southern SoG, however the summer northwesterlies do not show an ~~similar~~ along-axis variation as clearly. The along-axis dominance and seasonal directionality of these records is consistent with ~~both the established wind climatology synoptic groupings~~ and topographic steering discussed in Sec. 2.1 and provides a potentially significant physical driver for upwelling in the SoG. ~~Additionally, the seasonal variation between winter and summer is consistent with the winter storm activity of the region.~~

With the along-axis wind ~~climatology dominance and seasonality~~ established, we now turn our focus to the 5 year SalishSea-Cast nitrate and temperature records. We first examine these records ~~at the four representative horizontal grid locations shown~~

360 in Fig. 1 (colored stars). Two of these locations are located near the tidal mixing regions in the northern and southern SoG (Discovery Passage and Boundary Pass, respectively), and the other two are located along the eastern and western coastlines

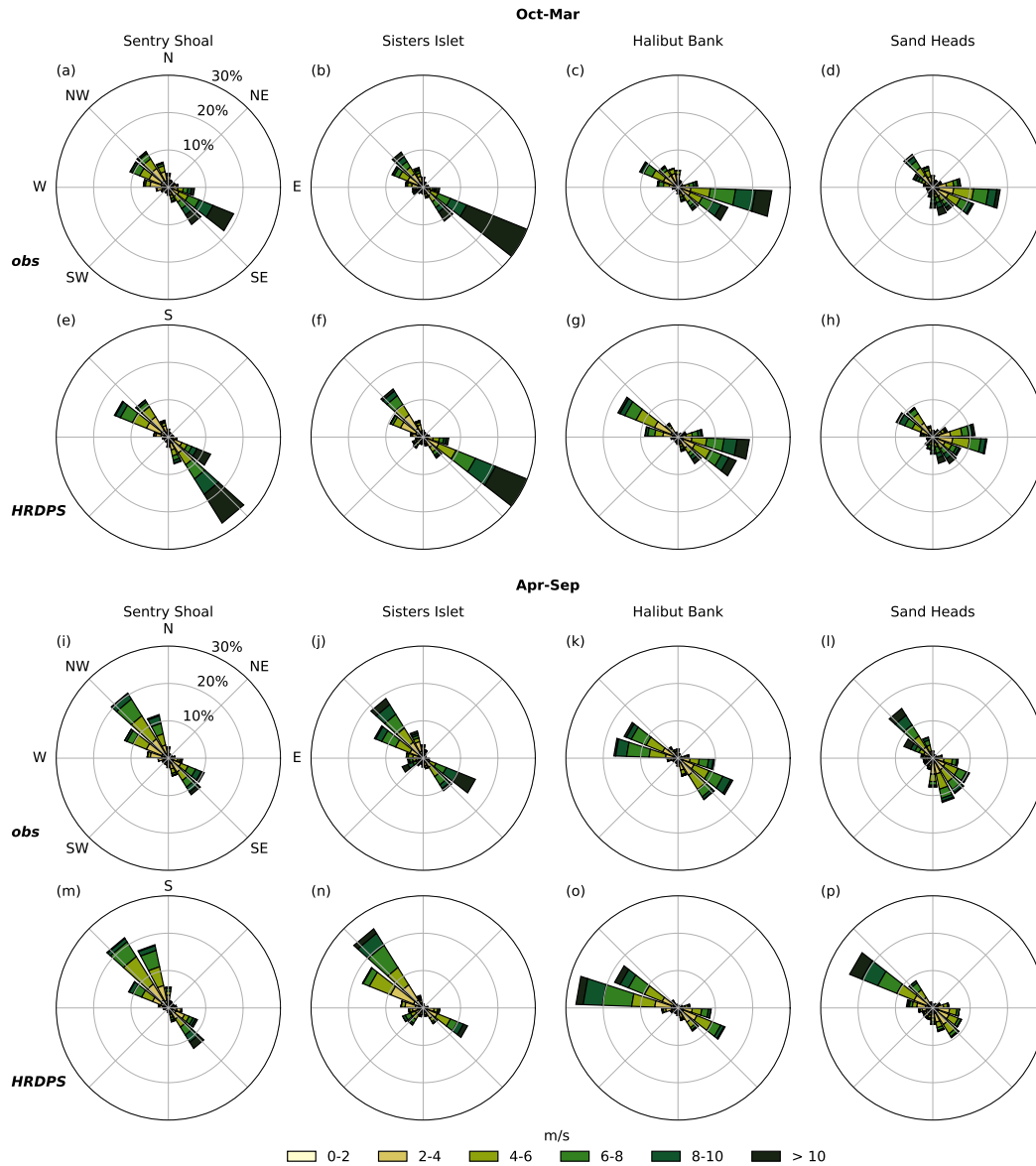


Figure 3. Condensed hourly wind station observations and hourly HRDPS results for the 2015 through 2019 period at Sentry Shoal (left column), Sisters Islet (second from left), Halibut Bank (second from right) and Sand Heads (right column). Data are binned by direction from and relative frequency of occurrence is given by the radial magnitude of each bin. Overall, the HRDPS wind record reproduces the observed, along-axis wind climatology at all stations. The seasonal wind separation of strong winter southeasterlies and weaker summer northwesterlies is also reproduced.

in the central SoG (Texada and Central VI, respectively). At all four locations, as spatial medians over an open water region of the domain and over two sets of grid points along the eastern Sunshine Coast and western Vancouver Island coast (Fig. 4a). Applying first a time median over the productive season to profiles of nitrate and temperature in the open water region, we demonstrate the seasonal vertical gradients, nitracline and thermocline respectively, that form in spring and erode in autumn (Fig. 4b). The nitracline is centered at approximately 5-15 m depth while the thermocline is shifted closer to the surface between 0 and 10 m depth. The small interquartile range for surface nitrate is consistent with continuous biological drawdown while the large interquartile range for surface temperature is indicative of more frequent sources of variability like diurnal heating and wind mixing.

365

370 Looking next at the surface, time series of median, open water surface nitrate and temperature exhibit seasonal cycles that follow the expected cycles of wind, solar and freshwater forcing described in Sec. 2.1 (Fig. 5, top panel). During winter when we anticipate elevated storm activity, surface nitrate is high and surface temperature is low. During summer when we

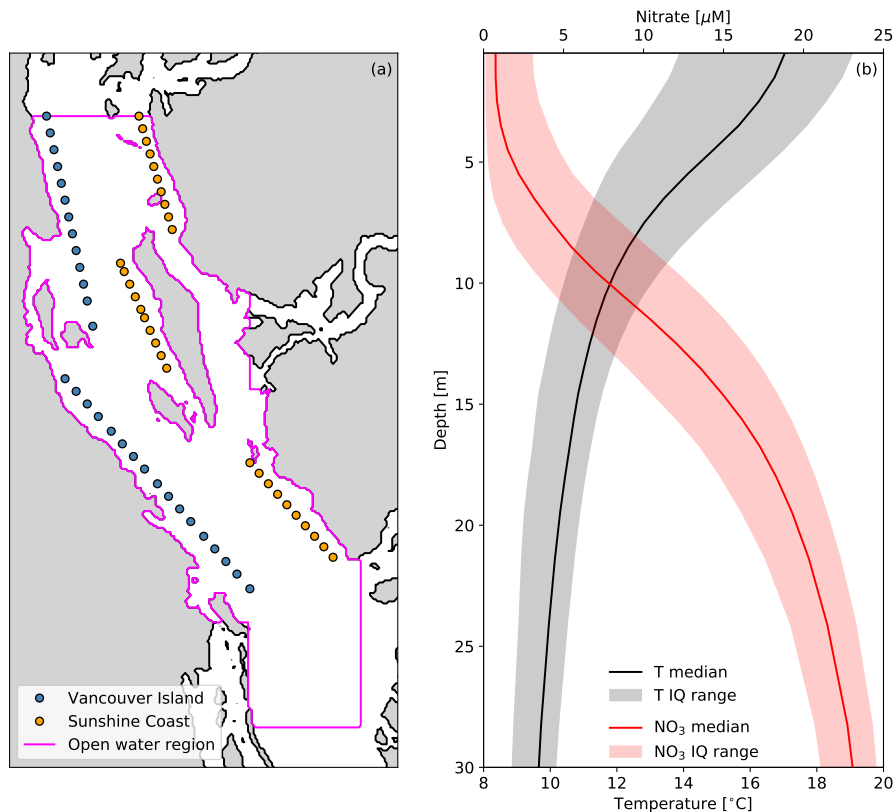


Figure 4. (a) Locations of grid points and regions used to obtain the spatial median time series of hourly temperature, nitrate and HRDPS along-axis wind speed shown in Fig. 5. (b) Time-median depth profiles of SalishSeaCast nitrate (NO₃, red line) and temperature (T, black line) during the productive seasons of 2015-2019 over the magenta open water region shown in (a). The seasonal cutoffs for each year are shown in Fig. 5 and the interquartile (IQ) range across all seasons is also shown (shaded envelopes).

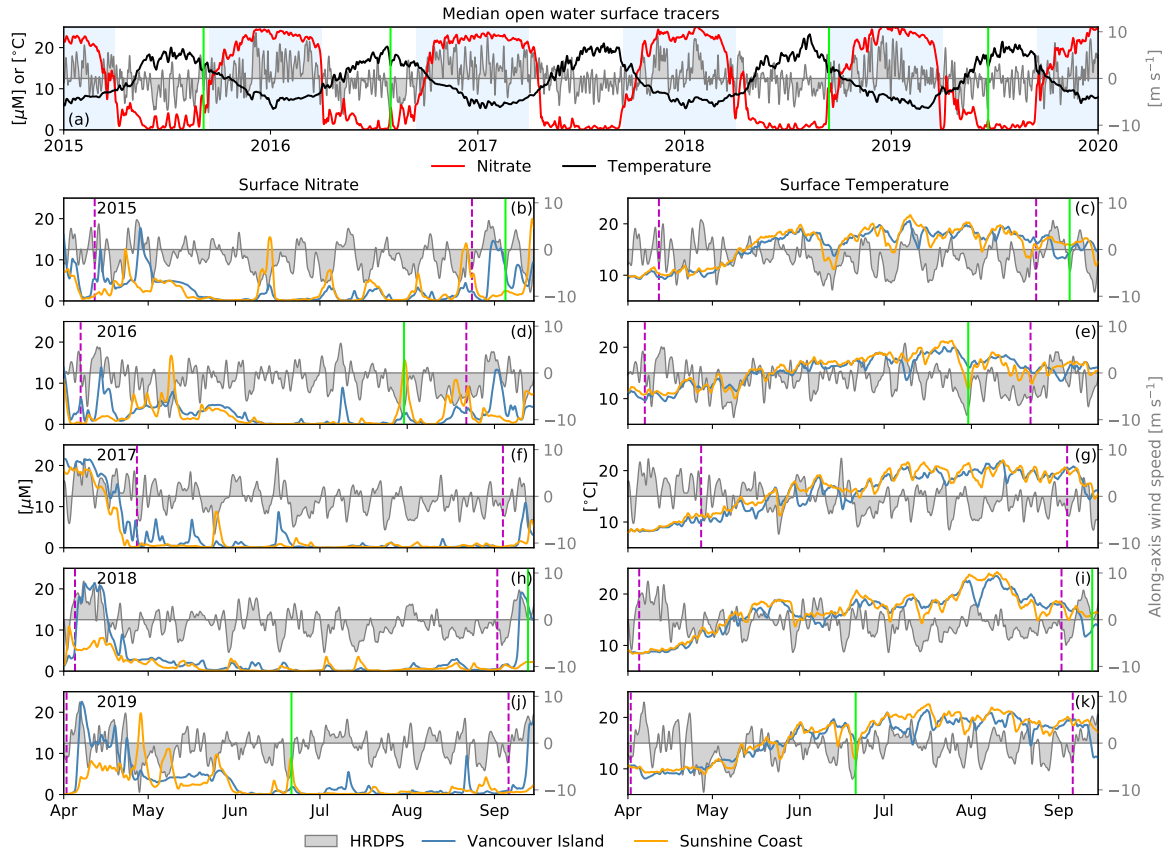


Figure 5. Time series of the SalishSeaCast hourly surface nitrate (left column) and surface temperature (right column) records during between 2015-2019 as spatial medians over (a) the open water region and (b-k) the coastal grid points shown in Fig. 4 at the 4 coastal locations shown in Fig. 1. The open water spatial median of HRDPS hourly along-axis surface wind speed record averaged over the Strait of Georgia region is also shown (gray patch). The nitrate, temperature and wind speed records have been low-pass filtered using a 3-day Blackman window to emphasize the subtidal variability. The 1 April to 15 September extent of the lower panels is indicated by the white regions in (a). The seasonal cutoffs bounding the productive season for each year (dashed magenta lines) and the dates of the four MODIS images shown in Fig. 2 (green solid lines) are also shown. Nitrate and temperature follow clear seasonal cycles, with higher frequency variability during the summer that visibly overlaps with wind variability. The Texada and Central Vancouver Island (VI) locations are positioned along the respective eastern and western shores of the Strait of Georgia where upwelling dominates, while the Discovery Passage and Boundary Pass locations are positioned at the northern and southern ends of the basin where tidal mixing dominates. The seasonal wind climatology between winter southeasterlies (positive) and summer northwesterlies (negative) is apparent from the spatially averaged HRDPS record. The characteristic biological summer surface nitrate drawdown is also apparent, and is interrupted by wind driven upwelling pulses at Central VI and Texada. The temperature cycle follows the solar heating cycle with cold, wind driven upwelling pulses at Central VI and Texada that co-occur with the nitrate pulses. Surface nitrate is never fully depleted in the tidal mixing regions.

anticipate strong stratification and biological nutrient uptake, surface nitrate decreases and surface temperature increases. The tidal mixing locations at Discovery Passage and Boundary Pass remain nitrate replete and cold throughout the summer, while the central locations at Texada and Central VI are more nitrate-depleted and warmer. The seasonality of wind speed and direction demonstrated in Fig. 3 is reflected in the spatial median of along-axis HRDPS wind speed averaged over the same open water region (Fig. 5, top panel, gray patch). Strong positive, or southeasterly, wind events dominate during the winter while weaker negative, or northwesterly, wind events dominate during the summer.

During the productive season, the spatial medians of surface nitrate and temperature along Vancouver Island and the Sunshine Coast exhibit significant episodic variations that overlap with corresponding variations in the along-axis wind record (Fig. 5, lower panels). The nitrate variability is clearly asymmetric between the two coasts, where variations along Vancouver Island are stronger during positive, or southeasterly, wind events while variations along the Sunshine Coast are stronger during negative, or northwesterly, wind events (Fig. 5, left panels). The episodic temperature variability is less clearly attributed to specific wind events or a given wind direction, and significant seasonal variability is still present within the productive season cutoffs (Fig. 5, right panels). However, the four MODIS surface temperature images and SalishSeaCast surface tracer snapshots presented in Fig. 2 overlap clearly with well-defined nitrate and temperature variations along the Vancouver Island coast in September 2015 and 2018 during southeasterly wind, and along the Sunshine Coast in July 2016 and June 2019 during northwesterly wind (Fig. 5, green lines).

Both surface nitrate and temperature fluctuate more strongly in summer compared to winter because of the seasonal vertical gradients, nitricline and thermocline respectively, that form in spring and erode in autumn. These gradients are visible in the seasonal median profiles of nitrate and temperature over the 5 year record at each of the four SalishSeaCast grid locations (Fig. removed, top row). The seasonal median window is defined according to the $2 \mu\text{M}$ nitrate threshold described in Sec. 2.2, and shown by the gray dashed lines in Fig. 5. Vertical gradients are weaker and shallower in the tidal mixing regions at Discovery Passage and Boundary Pass relative to the central locations at Texada and Central VI. At Texada and Central VI the gradients are stronger, however the nitricline is approximately 5-10 m deeper than the thermocline and the surface nitrate interquartile range is nearly zero while the temperature interquartile range is largest at the surface. These differences between the vertical structure of nitrate and temperature are consistent with the more episodic surface nitrate pulses relative to the more periodic surface temperature variations (Fig. 5). Additionally, the seasonal nitricline is established earlier than the seasonal thermocline since the spring diatom bloom precedes the period of maximum stratification and solar heating. This delay in thermocline development is reflected in the slow warming of the surface locations (Fig. 5, right column) relative to the rapid spring nitrate drawdown (Fig. 5, left column). There is also a small but significant cross-axis asymmetry where both the nitricline and thermocline are up to 5 m shallower on the eastern side of the basin at Texada relative to the western side at Central VI (Fig. removed b, c). This asymmetry is consistent with the cross-axis stratification gradient mentioned in Sec. 2.1.

Regardless of the differences between surface nitrate and surface temperature, large fluctuations in both quantities along the basin sides at Texada and Central VI overlap with directional wind events in a manner consistent with upwelling (Fig. 5). Specifically, nitrate pulses along the eastern shore at Texada occur during northwesterly wind events and nitrate pulses along the western shore at Central VI occur during southeasterly wind events. These events occur in the surface temperature record

as cold pulses. However, the periodic forcing mechanisms like tides and diurnal heating may also be embedded in these pulses to some degree and tides certainly dominate at Discovery Passage and Boundary Pass. Power spectra of the surface nitrate and temperature records at Discovery Passage and Boundary Pass indeed show clear amplitude peaks in the tidal frequencies as well as smaller but distinct peaks at the fortnightly and monthly frequencies (Fig. removed, bottom rows). These distinct peaks are largely absent at Texada and Central VI and the low frequency energy is more broadly distributed, with the major exception of a strong diurnal heating peak in the surface temperature spectra.

3.2 Principal component analysis

When principal component analysis is applied to the de-trended surface nitrate and temperature records resampled over the SoG subdomain shown in Fig. 1 during the seasonal nitrate threshold windows shown in Fig. 5, approximately, only the first three nitrate modes and the first temperature mode account for greater than 10% each of the total variance. Nearly half of the variance for each tracer is explained by the first 3 these modes (44.9% and 42.7% respectively for nitrate and temperature), with (Fig. 6). However, the variance distribution across these modes and the physical interpretation of the EOF spatial patterns is different for each record. For surface nitrate the variance is distributed approximately equal variance distribution across the three nitrate modes, which represent in order of decreasing variance, upwelling along the western shore (mode 1), tidal mixing near the basin ends (mode 2) and upwelling along the eastern shore (mode 3). When the same analysis is applied to surface temperature, a mixing-heating pattern dominates the variance (mode I) followed by two cross-axis patterns (modes II and III). The nitrate and temperature EOF modes can be considered as anomalies superimposed on the seasonal median surface fields (Figs. 6a and e). In this context, the small amplitude of the nitrate EOF mode 2 is a tidal modulation of the background elevated nitrate concentration in the tidal mixing regions. Conversely, the more wind and solar driven modes (nitrate modes 1 and 3, temperature mode I) have vanishing amplitudes in the tidal mixing regions. The nitrate and temperature For the remainder of this analysis, we reference these modes as nitrate modes 1, 2 and 3 and temperature mode I, and we disregard the higher modes that account for increasingly small fractions of the total variance.

Following the mode attribution criteria described in Section 2.3, we first examine the EOF spatial anomaly patterns for each mode (Fig. 6). The median surface nitrate and temperature fields are included to show the background state of each tracer (Fig. 6a and b). As expected from the median profiles shown in Fig. 4b, surface nitrate is depleted and surface temperature is high in the interior SoG, with each tracer respectively increasing and decreasing approaching the tidal mixing zones to the north and south. The nitrate mode 1 and 3 EOF patterns show clear coastal anomalies in the nitrate-depleted interior SoG, indicative of upwelling along the respective western and eastern coastlines. Conversely, the nitrate mode 2 EOF pattern shows no significant anomalies in the interior SoG, but instead an anomaly in the southern passages near Haro Strait indicative of fortnightly tidal mixing modulation. The temperature mode I EOF shows a uniform anomaly in the interior SoG, indicative of both wind mixing and diurnal heating and cooling. There is also a weak cross-axis gradient in temperature mode I that may indicate the partial influence of upwelling along the eastern coastline, similarly to nitrate mode 3.

We next examine the PC loadings time series for each mode, beginning with the primary upwelling candidates, nitrate modes 1 and 3 behave consistently with the physical interpretations of their EOF counterparts (Fig. 7). Both modes feature pronounced

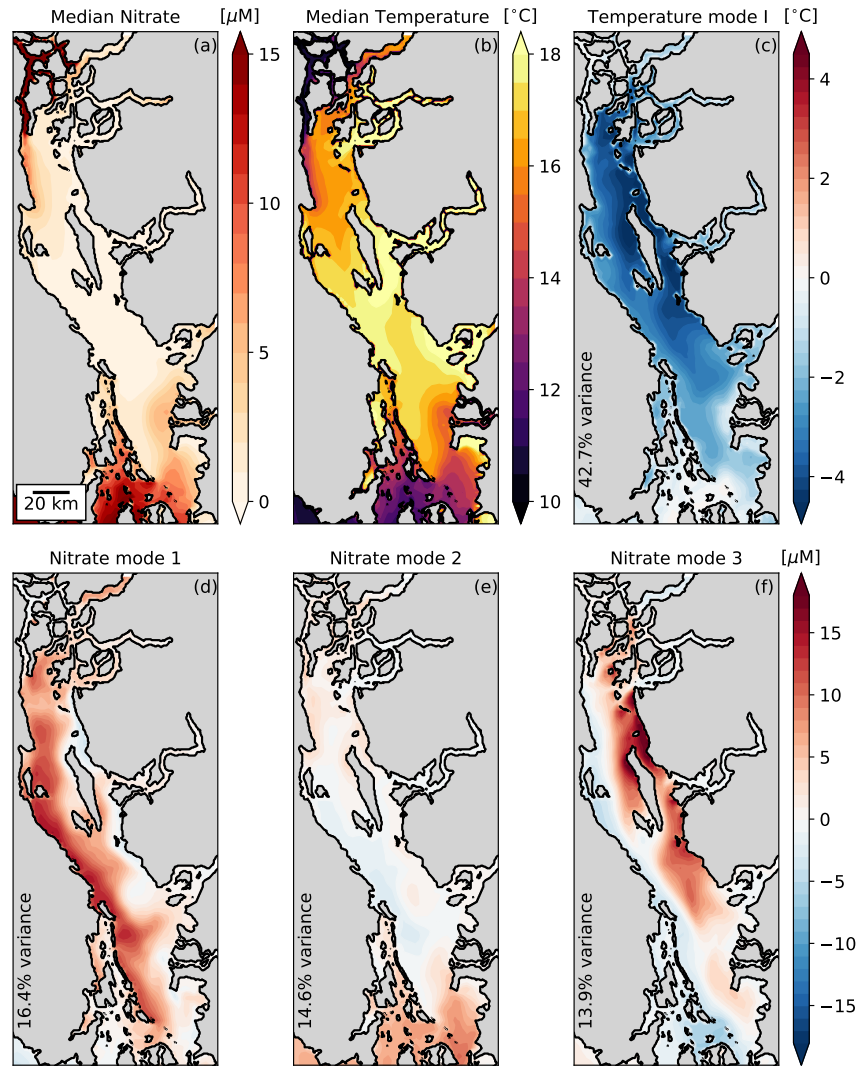


Figure 6. Empirical orthogonal function (EOF) modes spatial anomalies in order of decreasing percent variance applied to the 2015-2019 SalishSeaCast surface temperature (c) and nitrate (d-e) records between the seasonal cutoffs shown in Fig. 5. The median surface nitrate (a) and temperature (b) fields between the seasonal cutoffs are also shown. The surface fields are subsampled to 2.5 km resolution and detrended using a 35 d high-pass Blackman window filter prior to the principal component analysis (Section 2.3). The variance explained by each mode is printed in the lower left corner of each panel. Nearly half of the total variance is distributed approximately evenly across the first three nitrate modes (d-f) while a similar 42.7% of temperature variance is contained entirely within the first temperature mode (c). Two cross-axis modes and one tidal mode dominate the nitrate variance approximately equally (d-f) while the temperature variance is dominated by a single mixing-irradiance mode (c) followed by two cross-axis upwelling modes (f-h). Higher modes contain additional upwelling and tidal variability, however the percent variance of each mode is significantly reduced beyond the third mode.

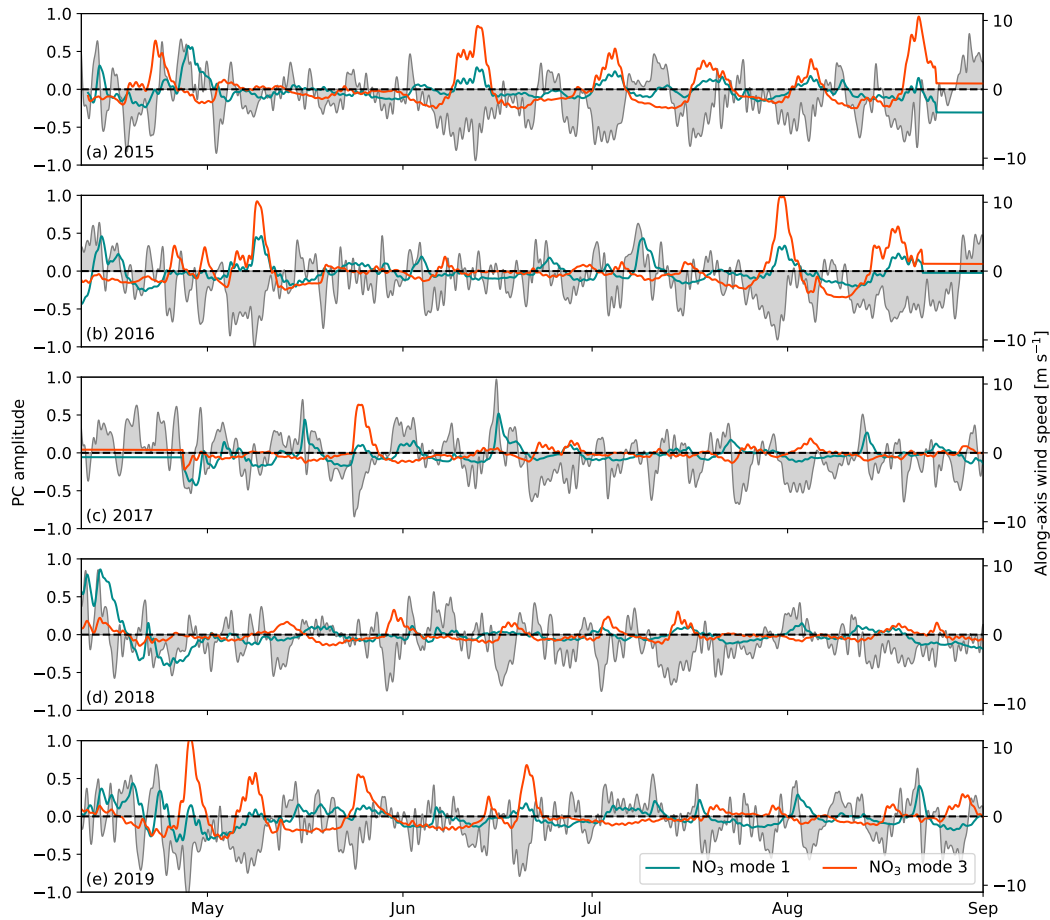


Figure 7. Time series of the first 3 principal component (PC) loadings for surface nitrate (left column) and temperature (right column) modes 1 and 3 corresponding to the EOF spatial patterns shown in Fig. 6. The spatial median of along-axis HRDPS wind speed averaged over the Strait of Georgia open water region in Fig. 4a (magenta region) is also shown. The PC and wind time series are low-pass filtered using a 1 d Blackman window cutoff in order to emphasize the low frequency variability. The PC loadings of both nitrate upwelling modes (NO₃ modes 1 and 3) increase in amplitude during sustained wind events while the tidal nitrate mode (NO₃ mode 2) is independent of wind entirely. The mixing-heating temperature mode (T mode 1) is positive during sustained wind and negative in the absence of wind when diurnal heating is most effective.

positive anomalies during wind events similarly to the medians along the coastal transects shown in Fig. 5. The western shore Nitrate upwelling mode 1 spikes increases during sustained positive along-axis, southeasterly wind events, while the eastern shore nitrate upwelling mode 3 spikes increases during sustained negative along-axis, northwesterly wind events. Nitrate modes 1 and 3 are not completely isolated in their wind responses, however. The mode 1 PC, for example, also weakly increases during northwesterly wind, which we also observed in the spatial median along Vancouver Island in Fig. 5. also weakly increases the amplitude of mode 1, likely through vertical mixing. Conversely, the tidal nitrate mode 2 demonstrates both high-frequency

and subtidal oscillations and no consistent overlap with the along-axis wind record. The dominant temperature mixing-heating mode I is positive (cold) during along-axis wind events in either direction and negative (warm) when the wind relaxes, with high frequency oscillations indicative of the diurnal heating cycle. The cross-axis temperature modes II and III are positive during northwesterly winds and negative during southeasterly winds, albeit less distinctly than the nitrate modes which is consistent with the larger interquartile range of temperature relative to nitrate near the surface (Fig. removed).

The PC loadings power spectra further support the periodicity observed in the PC loadings time series (Fig. 8, top rows). With respect to nitrate, tidal energy is primarily observed in mode 2, including pronounced fortnightly and monthly subtidal peaks. In the remaining Looking next at the power spectral density (PSD) of the PC loadings for each mode, the nitrate upwelling mode 1 and 3 only smaller tidal peaks are present and the primary energy is more and temperature mode I power spectra all show broadly distributed energy in the subtidal range, while the nitrate mode 2 PSD is more focused into the fortnightly and monthly subtidal bands (Fig. 8a). These power spectra suggest that nitrate modes 1 and 3 and temperature mode I are wind-driven while nitrate mode 2 is driven by the fortnightly tidal cycle. The nitrate mode 3 PSD also shows a distinct peak in the 15-20 d band (Fig. 8a, orange curve) that is consistent with the visual spacing of the mode 3 anomalies in Fig. 7. All four modes have significant peaks in the tidal range, indicating that tidal energy is never fully separated by the PCA method even when varimax rotation is used. We make no further distinctions about PSD in the tidal range, with the exception of the concentrated energy around the diurnal band in the temperature mixing-heating mode I spectrum (Fig. 8a, black curve) which is indicative of is similar to nitrate modes 1 and 3 with the exception of a pronounced diurnal heating and cooling signal. Temperature mode II is not easily categorized. The EOF pattern exhibits both a cross-axis gradient and significant anomalies in the tidal mixing region (Fig. 6g) while the spectral density shows strong tidal peaks and a broad distribution of subtidal energy (Fig. 8e). The temperature mode III EOF pattern is more clearly cross-axis (Figs. 6h) and the spectral density is more similar to the nitrate upwelling modes 1 and 3 (Fig. 8f), although the explained variance is lower at 6%.

All four PCA modes demonstrate some degree of significant spectral coherence with along-axis wind stress beyond the 99% confidence interval (Fig. 8b). Nitrate mode 3 is significantly coherent with wind stress across the subtidal frequency range with maximum coherence in the 15-20 d band, while the remaining modes are coherent only at discrete frequencies within the 2.5-10 d band. The increased coherence at lower frequencies for nitrate mode 3 is consistent with the visual spacing of the nitrate mode 3 PC anomalies in Fig. 7 and with the longer maximum duration of summer synoptic types mentioned in Section 2.1. Conversely, the higher frequency coherence bands for nitrate mode 1 are more consistent with the shorter maximum duration of winter synoptic types. Additionally, we have likely selected for the higher overall coherence observed in nitrate mode 3 by restricting our analysis to the productive season when northwesterly wind dominates. Nitrate mode 2 demonstrates significant coherence in the 3-10 d band, however since the mode 2 PSD is concentrated in the fortnightly and monthly bands, we do not associate this coherence with significant PC variability. Temperature mode I demonstrates the weakest coherence of all modes, which may simply be the result of a complicated response to both wind and solar forcing.

The time lag between a wind event and a corresponding PC anomaly can be estimated from the phase lag associated with the coherence calculation (Fig. 8c). Nitrate mode 2 is not shown since we have disregarded the significance of the coherence. Likewise, we have limited the nitrate mode 1 and temperature mode I lag estimates to the 2.5-9 d frequency range since

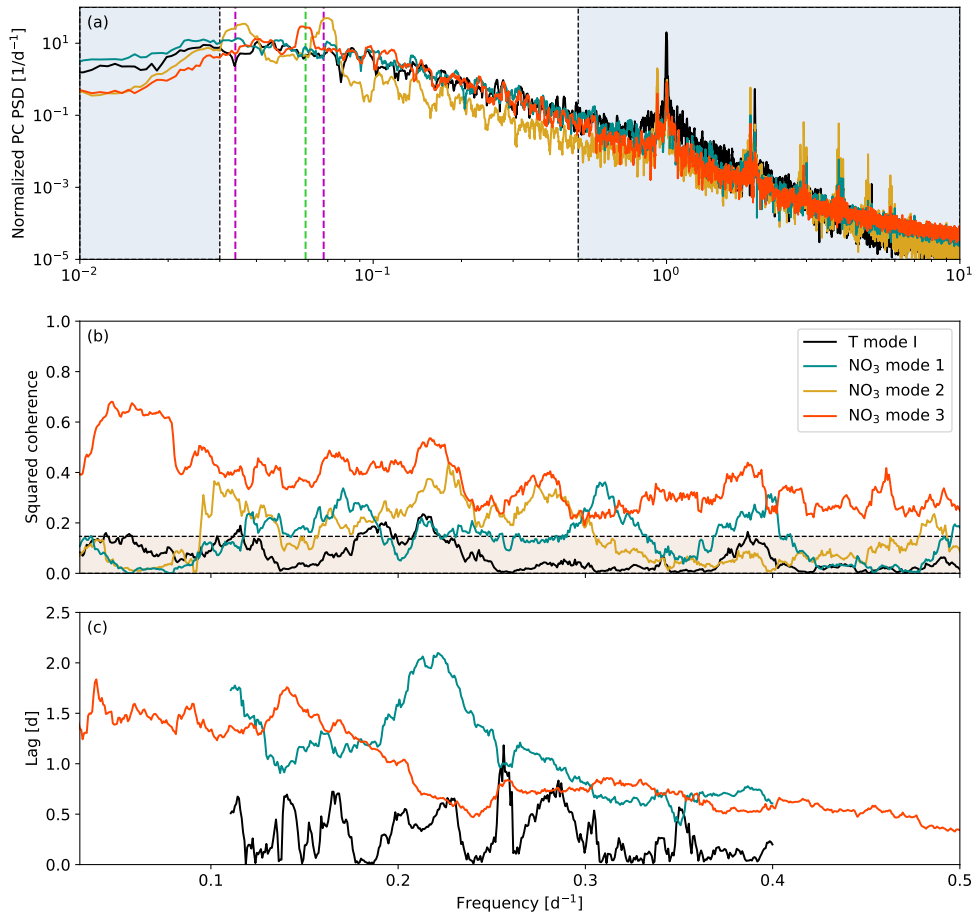


Figure 8. (a) Normalized power spectral density (PSD) of and (b) spectral coherence with along-axis, HRDPS wind stress calculated from the first 3 principal component (PC) mode loadings for surface nitrate (top row) and temperature (second from top) corresponding to the EOF spatial patterns of the four surface tracer PCA modes shown in Fig. 6. The phase lag associated with the coherence calculation is shown as a peak-to-peak time lag (c) for nitrate modes 1 and 3 and temperature mode I. The fortnightly and monthly subtidal diurnal and semidiurnal frequencies are shown as in (a) (magenta dashed lines), and a subtidal peak in nitrate mode 3 centered at 17 d is also shown (green dashed line). Panels (b) and (c) are shown on a linear frequency axis over the non-shaded region in (a). The 99% confidence interval for coherence is shown by the shaded region in (b). Peak-to-peak lags for nitrate mode 1 and temperature mode I are only shown in the 2.5-9 d band since neither mode is significantly coherent with wind stress beyond this range. The tidal energy in nitrate mode 2 is apparent (b) as is the diurnal heating signal in temperature mode I (d), while the subtidal energy in the remaining modes is more broadly distributed.

coherence for these modes is not significant outside of this range. We do not attempt to draw meaningful conclusions about the lag variability or frequency distribution. Instead we simply observe that the lags associated with nitrate modes 1 and 3 are similar and range between approximately 0.5 and 2 d while the lag associated with temperature mode I is shorter, ranging from

485

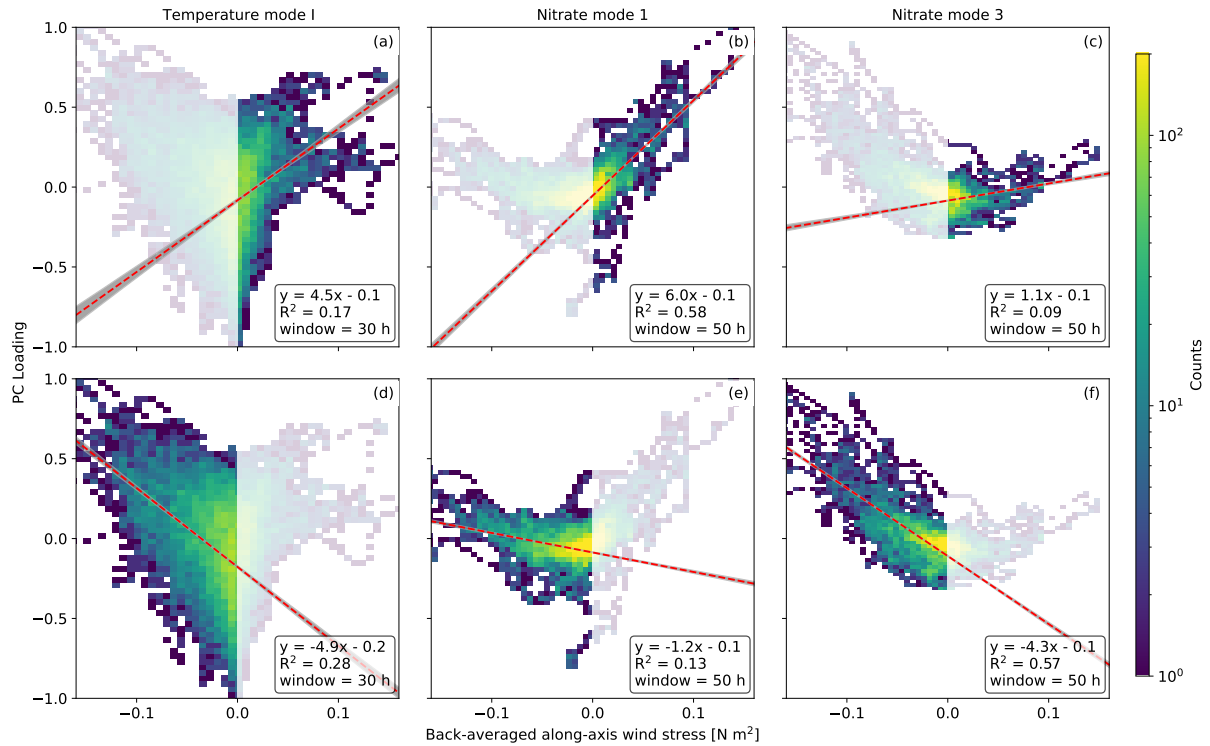


Figure 9. 2-D histograms of the PC loadings of nitrate (second from bottom) and for temperature (bottom) mode I (a, d), nitrate mode 1 (b, e) and nitrate mode 3 (c, f) versus the temporally back-averaged spatial median of along-axis wind stress calculated from spatial-averaged the HRDPS wind speed record according to Equation 2. Bayesian linear regression is performed separately for positive, southeasterly (a-c) and negative, northwesterly (d-f) wind stress. Regression statistics shown include a mean best fit (red line and equation), a 99% confidence interval (gray envelope), a correlation coefficient (R^2) and a wind stress back-averaging window tuned to maximize R^2 . The temperature mode I correlation is strongly symmetric between positive and negative wind stress, and the back-averaging window is approximately 30 h for both directions. Conversely, the nitrate modes 1 and 3 correlations are strongly asymmetric between wind stress directions, and the back-averaging window is thus determined according to the wind stress direction that yields the highest regression slope and R^2 value. This direction is positive for nitrate mode 1 (b) and negative for nitrate mode 3 (f), with a 50 h averaging window for both modes. The time averaging window is selected to maximize the Pearson correlation coefficient between the PC record and the wind stress. The correlation coefficients for nitrate modes 1 and 3 are determined using only the wind stress values with the sign of the dominant correlation direction. Correlations for nitrate mode 2 and temperature modes II and III are weak and thus not reported—a default back-averaging window of 48 h is used in those cases. Nitrate modes 1 (g) and 3 (i) are correlated, respectively, with positive and negative along-axis wind stress over a 54 h averaging window while temperature mode I (j) is correlated with the overall wind stress magnitude over a 30 h averaging window.

0-1 d. These estimates reflect the peak-to-peak lag between signals and thus do not account for the onset of a wind event which precedes the peak.

By evaluating The final mode attribution criterion described in Section 2.3 is the correlation between the PC loadings and the timeback-averaged along-axis wind stress, shown for the wind-forcing candidates, nitrate modes 1 and 3 and temperature mode I, in Fig. 9. All three modes increase with wind stress in both along-axis directions. We therefore calculate linear regression and the correlation coefficient R^2 for each mode separately for positive, southeasterly wind stress (Fig. 9a-c), and for negative, northwesterly wind stress (Fig. 9d-f). The minimum back-averaging window required to maximize the correlation between temperature mode I and either direction of wind stress is approximately 30 h. Nitrate modes 1 and 3 are more asymmetric in their correlation with wind stress, and we determine the minimum back-averaging window based on the sign of wind-stress that yields the stronger correlation. This sign is positive for nitrate mode 1 and negative for nitrate mode 3, with a window of approximately 50 h required to maximize the correlation for both nitrate modes. This longer window relative to the 30 h window determined for the temperature mode is consistent with the peak-to-peak lags that we observed in Fig. 8c.

Linear regressions for all modes against both positive and negative wind stress yield significant correlations, in that the probability distribution of each regression slope never contains zero within the 99% confidence interval (Fig. 9, grey envelopes). This significance combined with the EOF patterns, power spectra and coherence satisfies our criteria for attributing wind as a dominant forcing of these modes. The mean regression slopes and correlation coefficients provide a further basis for quantifying and interpreting the asymmetry between the southeasterly and northwesterly wind stress dependence of each mode. Nitrate mode 1 is strongly asymmetric with a significantly higher regression slope and R^2 for positive, southeasterly wind stress and nitrate mode 3 is similarly asymmetric but with stronger correlation statistics for negative, northwesterly wind stress. Conversely, temperature mode I demonstrates weaker asymmetry, with a marginally stronger correlation during negative, northwesterly wind.

Reviewing the mode attribution criteria described in Section 2.3, we attribute the following physical processes to each PCA mode. Based on the coastal nitrate mode 1 and 3 EOF anomalies, the broad distribution of subtidal spectral energy, the significant coherence with along-axis wind stress in the expected frequency ranges and the asymmetric correlation between positive and negative wind stress, we attribute nitrate modes 1 and 3 to upwelling along the respective western and eastern coastlines. Conversely, given the nitrate mode 2 EOF anomaly in the southern tidal mixing region, the concentration of spectral energy at the fortnightly and monthly frequencies, the lack of significant wind-stress coherence at these frequencies and the lack of wind stress correlation (not shown), we attribute nitrate mode 2 to changes in tidal mixing strength due to the fortnightly tidal cycle. Finally, based on the uniform temperature mode I EOF anomaly in the interior SoG, the broad distribution of subtidal spectral energy coupled with a pronounced diurnal peak and the symmetric correlation between positive and negative wind stress, we attribute temperature mode I to a combination of wind mixing and diurnal heating and cooling. Given these mode attributions, we conclude that subtidal surface nitrate variability during the productive season is dominated by upwelling and fortnightly tidal modulation while subtidal surface temperature variability is dominated by wind mixing and diurnal heating and cooling. Since tidal mixing anomalies are limited to the ends of the basin, we further conclude that upwelling is the dominant source of surface nitrate to the interior SoG during the productive season.

~~calculated from HRDPS wind velocity according to Equation 2, we formalize the wind dependence of each PCA mode (Fig. 9, bottom rows). Nitrate upwelling modes 1 and 3 demonstrate clear correlations to southeasterly and northwesterly~~

wind stress, respectively, while the tidal mode 2 does not correlate with wind stress at all. The Pearson correlation coefficients for modes 1 and 3 are determined using only the wind stress values with the sign of the dominant correlation direction. The small amount of correlation between these modes and the reverse wind stress directions, which we attribute to wind mixing, is thus excluded from the analysis. The correlation is further maximized by choosing a wind stress backward averaging window of 54 h. Since there is no significant correlation for nitrate mode 2, a default 48 h averaging window is used. With respect to temperature, mixing-heating mode I correlates positively (cold) with both northwesterly and southeasterly time-averaged wind stress — the absolute value of the wind stress is used to calculate the correlation coefficient in this case. The backward averaging window that maximizes the correlation coefficient for this mode is 30 h, which is 1 d shorter than the averaging window used for the nitrate upwelling modes. The cross-axis temperature modes II and III visibly correlate positive (cold) with northwesterly wind stress and negative (warm) with southeasterly wind stress. However, since these correlations are weak and the percent variances associated with these modes are low, we have not attempted to quantify the correlation and use the default 48 h wind stress backaverage for visualization only. While these weak correlations are indicative of wind dependence to some degree, the unclear EOF spatial patterns and PC spectra prevent us from drawing meaningful conclusions about modes II and III. Additionally, given the low percent variances explained by these higher temperature modes relative to mode I, we assign them secondary importance and do not discuss them further.

4 Discussion

4.1 Modes of Upwelling mechanisms

To provide a mechanistic context to the cross-axis upwelling response observed in the nitrate PCA results modes 1 and 3, we compare our results with two-layer shallow water theory in a closed basin. We consider a two-layer model to be sufficiently suited for describing upwelling across the pycnocline despite the established three-layer structure of the SoG since the deep layer is generally observed to be below 200 m depth (Pawlowicz et al., 2007). We also disregard the complicating factors of the stratified surface “mixing layer” (e.g., Collins et al., 2009) since the onset of sustained wind homogenizes this layer in SalishSeaCast in a matter of hours (simulations not shown) compared with the longer upwelling response that we determined during the mode attribution on the order of days. Additionally, upwelling solutions of two-layer problems retain many of their defining characteristics as additional layers are added (Csanady, 1982a).

Two layer model description

Consider a wind forced, two layer, linearized, shallow water approximation of a rectangular basin as described by Csanady (1982b). Assuming that baroclinic motions dominate the momentum balance, the lower layer transports are equal and opposite to the upper layer transports and the interface displacement ζ is coupled to the surface displacement η according to

$$\eta = -\frac{\Delta\rho}{\rho_0} \frac{h_1 + h_2}{h_2} \zeta \quad (8)$$

where $\Delta\rho$ is the density difference across the pycnocline, ρ_0 is the background density, and h_1 and h_2 are the respective upper and lower layer thicknesses retain their previous definitions from Equation 1. This coupling between the upper and lower layers results in a single set of momentum and continuity balances for the lower upper layer cross-axis and along-axis transports, U and V , respectively

$$\frac{\partial U}{\partial t} - fV = g'h_1\delta_h \frac{\partial \zeta}{\partial x} \quad (9a)$$

$$\frac{\partial V}{\partial t} + fU = g'h_1\delta_h \frac{\partial \zeta}{\partial y} + \delta_h \frac{\tau}{\rho_0} \quad (9b)$$

$$\frac{\partial U}{\partial x} + \frac{\partial V}{\partial y} = \frac{\partial \zeta}{\partial t} \quad (9c)$$

where x , y and t are the respective cross-axis, along-axis and time coordinates, f is the Coriolis parameter, $g' = g\Delta\rho/\rho_0$ is the reduced gravitational acceleration across the interface, g is the gravitational acceleration constant and τ is the along-axis wind stress and F_x and F_y are the cross-axis and along-axis bottom friction terms. The thickness ratio $\delta_h = h_2/(h_1 + h_2)$ determines the amount of coupling between the surface forcing τ and the lower layer motions. For a deep SoG, assume $h_1/h_2 \ll 1$ and $\delta_h \approx 1$. For the moment, we assume negligible bottom friction. as well, except in the case of the growing coastal jet that we will discuss shortly

The balance between the wind stress term and the pressure gradient force term is a recurring element in solutions to Equation 9. Assuming that the shear stress between layers translates directly from the surface wind stress, which is common in two-layer models of lakes (e.g., Stevens and Lawrence, 1997; Stevens and Imberger, 1996), this balance and can be summarized by the a bulk Richardson number $Ri = g'h_1\rho_0/\tau$. Additionally, there are three fundamental length scales to consider: the along-axis length L_A , the cross-axis length L_C and the internal Rossby deformation radius L_R , which is redefined from Equation 1 for our two-layer approximation as $L_R = \sqrt{g'h_1}/f$. Near a coastline, L_R represents the transition between pressure gradient dominance in the near-shore region and Ekman flux dominance in the offshore region. Naturally, if $L_C/L_R \ll 1$ then pressure gradients dominate everywhere and steady Ekman fluxes cannot develop.

Let us Here we explore two well-established solutions to Equations 9a-c in the context of a northerly wind event that drives upwelling along the eastern shore. simple cases for wind driven upwelling within this two layer model. Case 1 considers interface displacements along the sides and ends of the basin as infinite coast approximations. This case is analogous to either a dynamically wide basin with $L_C/L_R \gg 1$ or the early stages of the wind response before the surrounding coasts become significant. Case 2 considers interface displacements constrained by the presence of all four coastal boundaries. This case is analogous to either a dynamically narrow basin with $L_C/L_R \ll 1$ or the later stages of the wind response after the surrounding coasts become significant. For consistency, Assume that We orient our coordinates such that x increases to the east west, and y increases to the north south, with the southwest northeast corner defined by is located at $x = 0, y = 0$, Further define and τ as is positive southward (Fig. 10) or toward the north.

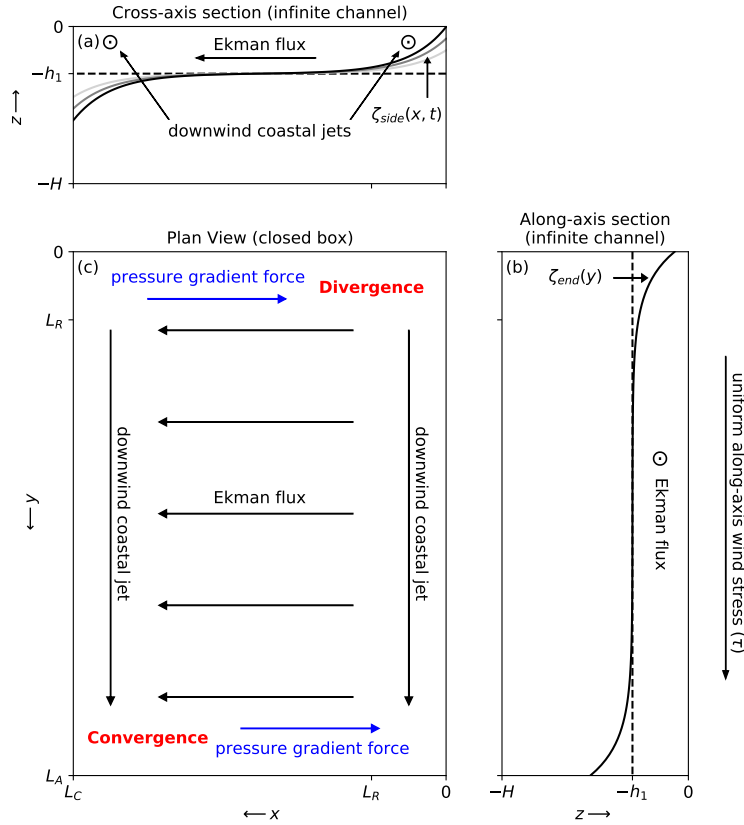


Figure 10. Diagram of the two-layer, infinite channel, interface displacement solutions in the (a) cross-axis and (b) along-axis directions, as forced by a uniform along-axis wind stress. The plan view (c) shows the surface divergence and convergence that are reasoned to occur when considering the infinite channel solutions in a closed basin.

Case 1: Upwelling along an Infinite coast channel solutions

Consider first the coasts along the sides of the basin at $x = 0$ and $x = L_C$ and neglect all along-axis gradients. After an initial spin-up period over which the cross-shore acceleration $\partial U / \partial t \rightarrow 0$, the surface wind stress drives a growing along-shore jets near the coastal $U = 0$ boundary conditions and a steady cross-shore Ekman flux far from the coasts where $\partial \zeta / \partial x \rightarrow 0$. Since the growing along-shore jets are in geostrophic balance with the cross-shore pressure gradient force, the interface tilt also grows with time. Assuming steady U and a linear time dependence for V , an approximate solution for ζ can be obtained is presented in Csanady (1973). The upwelling solution along the eastern shore is

$$590 \quad \zeta_{side}(x, t) = \frac{L_R}{Ri} f t e^{-x/L_R} \quad (10)$$

while a reversed downwelling solution arises along the western shore (Fig. 10a). The interface displacement at the coast is thus a linear function of ft determined by Ri and L_R .

Next consider the coasts at the upwind and downwind ends of the basin at $y = 0$ and $y = L_A$ and neglect all cross-axis gradients. After an initial spin-up period over which all accelerations $\partial U/\partial t \rightarrow 0$ and $\partial V/\partial t \rightarrow 0$, the surface wind stress balances a steady pressure gradient force near the end coasts and a steady along-shore cross-wind Ekman flux far from the end coasts where $\partial\zeta/\partial y \rightarrow 0$. The interface displacement only grows large enough to accommodate this pressure gradient force balance. Assuming steady U and zero V , an approximate solution for ζ can be obtained is also presented in Csanady (1973). The upwelling solution at the upwind end is

$$\zeta_{\text{end}}(y) = \frac{L_R}{Ri} e^{-y/L_R} \quad (11)$$

while a reversed downwelling solution arises along the downwind end (Fig. 10b). The interface displacement at the coast is once again determined by Ri and L_R but the solution is now steady with no continued growth. Comparing Equations 10 and 11, ζ_{side} clearly exceeds ζ_{end} for wind impulse durations longer than $t = 1/f$. Since $1/f \approx 2.5$ h at the SoG latitude while most upwelling-favorable wind events in the SoG persist from one to several days, ζ_{side} the time scales associated with the peak-to-peak lags and wind stress back-averaging windows are significantly longer, ζ_{end} is unlikely to contribute significantly to upwelling.

While the linear time approximation used to obtain ζ_{side} becomes increasingly invalid as upwelling progresses, the interface displacement presumably continues to grow by some unknown function of t until the coastal jet is balanced by bottom friction. This frictional adjustment period can be approximated by parameterizing the estimated by adding a quadratic bottom friction according to a simple quadratic drag law $F_y = -C_b (V/h_2)^2$ term to the lower layer counterpart of Equation 9b at the coast

$$\frac{\partial V_2}{\partial t} = -\frac{\tau}{\rho_0} - C_b \left(\frac{V_2}{h_2} \right)^2 \quad (12)$$

where V_2 is the lower layer along-axis transport and C_b is the bottom drag coefficient. The Coriolis term has vanished due to the coastal boundary condition and the along-axis pressure gradient has been neglected. A solution for Substituting F_y into Equation 9b and solving for V_2 at the coast gives is presented by Csanady (1974) and decays with time over an e -folding time scale of $T_F = h_2/\sqrt{4C_b\tau/\rho_0}$ (Csanady, 1974). For a typical drag coefficient of $C_b = 2 \times 10^{-3}$ and a nominal lower layer thickness of $h_2 = 100$ m, a wind stress of $\tau = 0.2$ N m⁻² corresponding to a wind impulse of approximately 10 m s⁻¹ produces a T_F on the order of approximately 1 d. This estimated frictional adjustment period is again smaller than the duration of a typical wind impulse in the SoG upwelling time scales suggested by our PCA results, however T_F is still approximately an order of magnitude larger than the inertial time scale that governs ζ_{end} .

Case 2: Upwelling in a Effects of the closed basin

The infinite coast channel approximations ignore a fundamental mass conservation discontinuities at the upwind ends of the basin where $x, y = 0$ and $x, y = (L_C, L_A)$. The downwind coastal jets along the sides of the basin at $x = 0$ there is a growing downwind coastal jet and along the end of the basin at $y = 0$ there is a steady combined with the cross-wind Ekman flux in the basin interior to the right of the wind in the positive x direction. The result in surface divergence and convergence at the respective upwind and downwind corners when the domain becomes closed (Fig. 10c). While simple analytical solutions that

625 resolve these discontinuities are difficult to obtain, we can reason that these divergences will ultimately cause the interface to lift upward and shoal at $x, y = 0$ and deepen at $x, y = (L_C, L_A)$ beyond what is described in the channel solutions.

Eventually, the surface tilts that accompany these interface displacements (Equation 8) will produce a cross-axis pressure gradient forces that Similarly, at the downwind end of the basin at $x = L_C$ and $y = L_A$, there is a surface convergence and interface depression. As these cross-axis pressure gradients begin to oppose the cross-axis Ekman fluxes near the ends of the basin (Fig. 10c, blue arrows), allowing downwind surface transport is no longer confined to within L_R of the ends and an along-axis interface tilt begins to emerge. These discontinuities exist even if $L_C/L_R \gg 1$, in the basin interior. As these If the cross-axis pressure gradients produced by the upwind corner divergence and downwind corner convergence propagate continue to develop along the entire length of the basin, they will eventually shut down all cross-axis Ekman fluxes. At this point, the along axis pressure gradient force will be the only term remaining to balance the wind stress once steady state is reached, and the resulting along-axis interface tilt can be described by the familiar wind setup equation Solving this reduced Equation 9b for ζ between the end walls at $y = 0, L_A$ gives

$$\zeta_{\text{setup}}(y) = \frac{L_A/2 - y}{Ri} \quad (13)$$

Equation 13 describes the classic along-axis pycnocline setup observed in narrow lakes (Stevens and Lawrence, 1997). As in Case 1, The interface displacement at the basin ends is now determined by $L_A/2Ri$. however the length scale has now increased significantly from L_R to $L_A/2$. In the SoG, $L_A/2$ is approximately an order of magnitude larger than L_R which makes Comparing this lake setup to the cross-axis channel solution, $\zeta_{\text{side}} = \zeta_{\text{setup}}$ when $t = L_A/2fL_R$. In the SoG, this required time is of similar order to the frictional time scale estimated above, which suggests that, if the lake setup were ever fully achieved, then ζ_{setup} and ζ_{side} would be of similar order as well.

The scenario we have presented to account for this along-axis, lake setup in the SoG relies on the basin being completely closed. In reality, the SoG is not closed but is instead connected to neighboring basins by complicated networks of passages. Given the presence of these passages, ζ_{setup} is unlikely to contribute significantly to upwelling relative to ζ_{side} , and the cross-axis upwelling described by ζ_{side} is ultimately what we observe in the raw hindcast surface tracers and in the PCA results. One major exception to this interpretation is the along-axis gradient in the nitrate PCA mode 3 coastal anomaly, which indicates that nitrate upwelling along the Sunshine Coast is consistently stronger in the northern SoG relative to the southern SoG. This regional upwelling pattern is consistent with at least a partial development of the corner divergence model in Fig. 10c. However, as we will discuss, there are other regional considerations that may explain this upwelling pattern as well.

The along-axis interface displacement evolves as an internal seiche over a time scale $L_A/(2e)$, or one quarter of the fundamental seiche period, where $e = \sqrt{g'h_1\delta_h}$ is the internal wave speed. However, the cross-shore pressure gradient at the upwind end of the basin driven by the corner divergence must first develop before the seiching begins, and this time scale is L_C/e . The complete time scale is thus $T_{\text{setup}} = (L_A/2 + L_C)/e$. At the scale of the SoG, T_{setup} can range from one to several days depending on $\Delta\rho$ and h_1 , as they pertain to e . In the real SoG, T_{setup} is likely at the long end of the estimated range because e is likely slower than the shallow water estimate for reasons that will be discussed in Section 4.3.

Considering the scale of the SoG, the overall upwelling response to wind forcing could be described by both Equation 10 and Equation 13 during the respective early and later stages of the wind impulse. The transition from ζ_{side} to ζ_{closed} could theoretically occur as early as one day after the wind onset, or T_{setup} could simply be too long to permit an observable transition at all. The PCA results suggest the latter, specifically that upwelling along the sides of the SoG is the dominant regime and any end effects are weakly significant at best.

4.2 Other geographic considerations

There are two secondary features specifically in the nitrate EOF mode 3 spatial pattern that require additional consideration. The first feature is the significantly stronger nitrate anomaly in the northern SoG relative to the southern SoG along the eastern coastline (Figure 6d). In the theoretical context discussed in Section 4.1, we suggested that this along-axis asymmetry surface nitrate anomaly gradient in PCA mode 3 EOF pattern could be interpreted as the result of a partial influence development of the corner divergences that we proposed to occur in a completely closed narrow-basin regime summarized by Equation 13. However, this asymmetry anomaly gradient is also overlapped by the an along-axis stratification gradient produced by the Fraser River plume (Masson and Peña, 2009). The effect of this stratification gradient on upwelling strength is demonstrated to first order through the bulk Richardson number dependence identified in Equation 10. Since interface displacement is inversely proportional to the density difference across the interface $\Delta\rho$, we expect the weakly stratified northern SoG to experience stronger upwelling than the strongly stratified southern SoG, especially near the Fraser River plume region. In fact, we observe the surface nitrate anomaly in the EOF mode 3 spatial pattern to vanish nearly completely within approximately 20 km of the Fraser River mouth.

For comparison, the western coastline nitrate upwelling EOF PCA mode 1 EOF that we attributed to upwelling along the Vancouver Island coast does not exhibit such striking along-axis asymmetry (Figure 6d). The greater uniformity of this anomaly may simply be due to the weaker overall stratification and nitracline present during the shoulder seasons. However, another consideration is that the In this case, the Fraser Plume is upwind while the downwind coastline is weakly stratified due to the tidal injection that propagates south from Discovery Passage (Olson et al., 2020). Additionally, an along-axis interface tilt due the narrow-basin regime described above is oriented in the opposite direction during the southeastly wind that drives upwelling along Vancouver Island, and if present, would now deepen the pycnocline along the downwind coastline and mitigate the effects of the weaker stratification in the north.

The second feature of the nitrate EOF mode 3 spatial pattern EOF not fully explained by cross-axis upwelling is the surface nitrate anomaly throughout the western Discovery Islands (Figure 6f). While significantly weaker than the coastal upwelling anomaly, this island signal none-the-less warrants special consideration given the ecological importance of the Discovery Islands habitat. At the southern opening of these island channels, the nitrate anomaly appears to be a northern extension of the cross-axis upwelling signal. Inside the channels however, the nitrate anomaly is more uniform and less visibly associated with any particular shoreline. A previous analysis of surface nitrate using SalishSeaCast in this region found this wind-driven nitrate signal to contribute significantly to summer monthly standard deviations during 2016 and suggested the most likely source was advection of tidally-mixed nitrate from the northern passages (Olson et al., 2020). Given the high median surface nitrate that

we observe in the northern passages of the Discovery Islands from our hindcast analysis (Figure 6a), we concur that southward advection of this persistent surface nitrate reservoir is a more accessible source of surface nitrate to the southern Discovery Islands than vertical mixing alone.

695 4.3 Comparison to other study regions

As mentioned in the introduction, the ~~modes of upwelling solutions~~ discussed above in Section 4.1 have been clearly demonstrated in several well-studied systems across a range of dynamic ~~scales widths~~. Specifically, cross-axis upwelling (Equation 10) dominates in dynamically wide basins like the Baltic Sea sub-basins (Bednorz et al., 2019) and in the North American Great Lakes (Plattner et al., 2006) while along-axis upwelling (Equation 13) dominates in dynamically narrow basins like the glacial
700 reservoirs of British Columbia (Stevens and Lawrence, 1997). In the SoG where L_R approaches the basin width, the ~~dynamic scale falls somewhere between these~~ dominant upwelling regime is less predictable. For context, the SoG is only narrower than Lake Ontario or the Gulf of Finland by approximately half. However, the SoG is also significantly more stratified due to the high salinity gradients and thus has a significantly larger L_R . Ultimately, L_R in the SoG is never larger than half the basin width, and upwelling falls clearly into the cross-axis regime of a large basin according to the PCA results. The $L_C/L_R = 1$
705 transition has been explored in fjords using an infinite channel approximation (Cushman-Roisin et al., 1994), but this exercise neglects the importance of the corner divergences ~~that we propose in Case 2 discussed earlier~~. Given the open passages at the ends of the SoG, perhaps an infinite channel approximation is indeed appropriate.

A striking contrast between the wind-driven pycnocline displacements in the SoG relative to the other systems discussed is the absence of basin-scale internal waves or seiches in our PCA results. Kelvin waves are an established wind response in large
710 lakes including Lake Ontario (Csanady, 1977), Lake Geneva (Bouffard and Lemmin, 2013), Lake Iseo (Valerio et al., 2012) and Lake Tahoe (Roberts et al., 2021) while the presence of along-axis seiches in narrow lakes is well documented (Laval et al., 2008; Stevens and Lawrence, 1997). ~~We attribute~~ This absence of detectable wave responses is possibly due to enhanced dissipation or damping as waves travel along the irregular coastline along the entire circumference of the SoG. Coastline irregularities have been demonstrated to significantly attenuate Kelvin wave amplitude and phase speed along continental
715 margins (Mysak and Tang, 1974) and complete damping of along-axis seiches has been documented in the Nechako Reservoir (Imam et al., 2013). More conclusively, SalishSeaCast simulations using a smooth geometric bathymetry produce Kelvin wave-like rotating seiches excited by the cross-axis upwelling response that are absent when the realistic bathymetry is used (simulations not shown). ~~In the context of Section 4.1 and Equation 13, the set-up time T_{setup} ignores the effects of dissipation and damping on the internal wave speed and the real time scale is likely much longer. We thus suggest that the dominance~~
720 ~~of cross-axis upwelling observed in the PCA results is at least partially due to the interactions between seiches and complex topography.~~

4.4 Ecosystem implications

Our findings suggest that surface nitrate supply in the SoG during the productive season is primarily ~~concentrated~~ sourced along the eastern and western coastlines and is stronger in the north relative to the south. While phytoplankton in the SoG are

725 extensively sampled and studied, finding consistent patterns between observed phytoplankton biomass and these surface nitrate anomalies presents several challenges. One such challenge is that ~~the along-axis phytoplankton distribution is seasonal chlorophyll averages are~~ already ~~strikingly asymmetric unevenly distributed~~ due to the along-axis stratification gradient. Specifically, surface chlorophyll is generally higher in the strongly stratified southern SoG and generally lower in the weakly stratified northern SoG (Suchy et al., 2019; Masson and Peña, 2009). This surface chlorophyll gradient alone is opposite what we would
730 expect given the enhanced northern nitrate upwelling revealed in this study. However the chlorophyll depth distribution is also ~~wider~~ larger in the northern SoG, with the highest depth-integrated biomass between Texada Island and Vancouver Island during the summer (Masson and Peña, 2009). More recently, an analysis of 5 years of sampled nitrate and chlorophyll profiles collected as part of the Pacific Salmon Foundation (PSF) Salish Sea Marine Survival Project revealed no significant along-axis spatial trends at the seasonal level (Pawlowicz et al., 2020). Given the comprehensive spatial and temporal coverage of this
735 data set, this finding suggests that the northern-intensified upwelling that we observe does not significantly affect chlorophyll at the seasonal level. Rather, an event-based analysis of such a data set is likely necessary to provide additional detail into the along-axis chlorophyll response to wind driven nitrate upwelling.

A second challenge is that nitrate upwelling events are episodic by nature and strongest near the shoreline, while nutrient and chlorophyll sampling are historically cruise-based and generally clustered toward the central axis of the SoG (Masson
740 and Peña, 2009). Such a sampling program is effective for tracking seasonal cycles and interannual variability throughout the SoG, but may entirely miss systematic chlorophyll anomalies that appear during nitrate upwelling along the coast. More spatially comprehensive data sets like the PSF data set present an opportunity to resolve these chlorophyll anomalies, however no analysis of this data set with an emphasis on the nearshore areas of the northern SoG has been completed to date. Perhaps these upwelling-driven chlorophyll signals can be resolved in future sampling programs and modeling studies that specifically
745 target these areas of enhanced nitrate upwelling.

Although nitrate is used as the primary upwelling tracer in this study, sub-pycnocline water is also associated with aragonite undersaturation and is thus potentially stressful for sensitive organisms such as shellfish. The two regions of particularly concentrated shellfish aquaculture activity identified in this study, Baynes Sound and the Discovery Islands, are both partially impacted by the wind-driven surface nitrate ~~mode 1 and 3 EOF anomalies that we found in EOF modes 1 and 3~~. Baynes
750 Sound in particular is centrally located along the Vancouver Island upwelling region (Figure 6d), and we reasonably expect this area to be impacted by sub-pycnocline water during southeasterly wind events. Conversely, the Discovery Islands are located outside of the main upwelling areas and we have stated previously that the nitrate anomalies that we observe in the EOF spatial fields in this region are ~~primarily likely~~ the result of surface advection. Continuous sampling at a shore station on Quadra Island maintained by the Hakai Institute has demonstrated rapid changes in temperature, salinity and aragonite
755 saturation state immediately following strong northerly wind events (Evans et al., 2018). While the authors determined that wind energy input was sufficient to vertically mix the water column to the depth required to produce these changes, given the persistent southward surface velocities that accompany these wind events (Olson et al., 2020) we still argue that lateral advection likely plays a significant role in these water property changes.

4.5 Limitations

760 The dominant PCA modes that we considered for surface temperature and nitrate accounted for less than half of the total variance associated with each de-trended tracer record, with the remaining variance spread across many higher modes of no clear physical attribution. Additionally, the dominant modes that we did examine contained significant energy at the tidal frequencies regardless of attribution. Ultimately, the PCA method only captured approximately 45% of the variance into easily interpretable modes and did not separate all of the tidal variability into higher modes only. In experiments where PCA was
765 performed on records that were lowpass-filtered to remove the tides in addition to the de-trending step, the fraction of explained variance for nitrate modes 1-3 increased to approximately 60%. This increase suggests that some of the unresolved, higher-mode nitrate variance is indeed tidal, however a similar increase was not achieved for temperature.

~~Based on the correlation between along-axis wind stress and the PC loadings time series, we have determined that the cross-axis surface nitrate gradients revealed by EOF modes 1 and 3 are produced by wind-driven upwelling. We have also
770 identified two potential features that might explain the along-axis nitrate variability in EOF mode 1: an along-axis pycnocline tilt and an along-axis stratification gradient. However, identifying with certainty which of these features influences the along-axis upwelling gradient with any significance is beyond the capability of this analysis. Specifically,~~

Since ~~in this contribution~~ we have limited our ~~data selection analysis~~ to surface wind, nitrate and temperature fields ~~only~~, we cannot draw further conclusions about the density structures that we have proposed to explain our PCA results, specifically
775 whether the along-axis pycnocline tilt required to enhance the strength of upwelling in the north actually occurs ~~or whether an along-axis stratification gradient indeed significantly affects~~ Furthermore, ~~while we have related stratification and pycnocline depth to the strength of upwelling through the bulk Richardson number, we cannot quantitatively constrain this relationship using surface nitrate anomalies alone.~~ Additionally, we have neglected other geographic features that have been suggested to influence upwelling strength such as cross-shore bottom slope (Choboter et al., 2011; Lentz and Chapman, 2004). For example,
780 along-shore variations in bottom slope have been implicated in observations of spatially persistent upwelling hotspots in the Gulf of Finland (Delpeche-Ellmann et al., 2018). ~~While explorations of pycnocline and nutricline depth changes are beyond the scope of the present study, they~~ Analysis of the density structure presents a logical next step for addressing these remaining questions ~~furthering our understanding of wind-driven upwelling and the impacts on surface nutrient supply and carbonate chemistry in the SoG.~~

785 From a more biological perspective, we have also neglected to quantify the primary productivity associated with the surface nitrate sink and instead assumed an overly simplistic pathway between nutrient availability and phytoplankton consumption. One potential consequence of this assumption relates again to the along-axis stratification gradient and the chlorophyll depth distribution that arises. Any complex interactions in the NPZD model involving light limitation and variability in growth and grazing rates that accompany this along-axis chlorophyll distribution and their effects on nitrate consumption would be
790 overlooked by our study. Previous studies that identify elevated chlorophyll biomass near regions of enhanced surface nutrient supply in the SoG such as tidal jets (Olson et al., 2020) and fronts (Parsons et al., 1981) suggest that upwelling-sourced nitrate

would indeed boost primary productivity as well, and we thus find our results promising. However, an integrated biophysical study that considers the fate of upwelled nitrate is another logical next step in addition to exploring the density structure.

5 Conclusions

795 We analyzed 5 years of hourly, high resolution surface nitrate and temperature results from the SalishSeaCast biophysical coupled model along with hourly, high resolution surface wind forcing fields from the operational Canadian HRDPS weather model in order to better characterize the mechanism of wind driven surface nutrient delivery in the SoG. We found the **primary dominant** HRDPS surface wind **climatology patterns** to be oriented **primarily** along the main axis of the SoG, with strong southeasterlies dominating in the winter and weaker northwesterlies dominating in the summer. These primarily along-axis winds
800 **climatology** produce **periodic episodic** upwelling along the Vancouver Island coast during the spring and fall and along the British Columbia mainland coast during the summer. This upwelling response produces clear surface nitrate and temperature anomalies along these coasts ~~and these anomalies are largely absent near the ends of the SoG where tidal mixing dominates.~~

Using principal component analysis (PCA), we determined that the cross-axis upwelling patterns in surface nitrate account for a combined $\sim 30\%$ of the variance across the 5 year record ~~with the non-productive season, including winter, removed~~
805 ~~during the productive season between the spring and fall phytoplankton blooms.~~ By sharp contrast, nearly half of the surface temperature variance over the same period is dominated by a single **combined** mixing **and diurnal** heating-cooling pattern. The **power spectra of these** principal component (PC) loadings time series **along with the spectral coherence and correlation between the PC loadings and the spatial median of** ~~for these modes correlate consistently with time-averaged~~ along-axis wind stress calculated from the HRDPS wind record ~~were used to confirm these physical attributions.~~ For surface nitrate, a positive
810 coastal nitrate anomaly band occurs to the **right left** of the wind stress direction. For surface temperature, strong wind stress in either direction occurs with cool anomalies while weak wind stress occurs with warm anomalies. We attribute this contrast between surface nitrate and temperature to a deeper nitracline relative to the thermocline. Under northwesterly winds, the nitrate upwelling anomaly along the eastern coastline is significantly stronger in the northern SoG relative to the south.

The cross-axis upwelling response revealed by the PCA results is consistent with basins that are wider than the baroclinic
815 Rossby deformation radius, and contrasts with the end-to-end pycnocline setup observed in narrow lakes. However, an along-axis pycnocline tilt is theoretically possible in the SoG due to a divergence at the upwind corner of the basin. Such a tilt would be consistent with the along-axis nitrate anomaly gradient along the eastern shoreline, although the background along-axis stratification gradient driven by the Fraser River could also explain this northern intensification of the surface nitrate anomaly. Regardless of the mechanism, this enhanced upwelling has implications for summer productivity in the northern
820 SoG. Sampling biases toward the open water regions of the SoG may prevent the impacts of this nitrate upwelling source from being observed. Overall, the episodic nature of upwelling in the SoG may disrupt the background state of coastal habitats, whether from a nutrient perspective for bottom-up control of higher trophic levels or from a $p\text{CO}_2$ perspective for sensitive shellfish aquaculture regions such as Baynes Sound and the Discovery Islands.

Code and data availability. All postprocessing and analysis scripts are available from the SalishSeaCast GitHub repository (https://github.com/SalishSeaCast/SoG_upwelling_EOF_paper). SalishSeaCast and HRDPS results are available from the SalishSeaCast ERDDAP server (<https://salishsea.eos.ubc.ca/erddap/griddap/index.html>). All observational data used in this study are available online from their respective organizations: Environment and Climate Change Canada (ECCC) meteorological station observations (https://climate.weather.gc.ca/historical_data/search_historic_data_e.html), Fisheries and Oceans Canada (DFO) buoy observations (<https://www.meds-sdmm.dfo-mpo.gc.ca/isdm-gdsi/waves-vagues/data-donnees/index-eng.asp>) and NASA MODIS Aqua images (<https://oceancolor.gsfc.nasa.gov/cgi/browse.pl?sen=amod>). More information about SalishSeaCast can be found on the project web page (<https://salishsea.eos.ubc.ca>). [Meteorological observing platform data may also be found via the Canadian Integrated Ocean Observing System \(CIOOS, <https://cioospacific.ca>\)](#).

Author contributions. BMM performed the analyses and drafted the manuscript. SEA performed the hindcast simulations of SalishSeaCast. Both authors contributed equally to the development of the research concept and the manuscript beyond the initial draft. BMM is supervised by SEA.

835 *Competing interests.* The authors declare that no competing interests are present.

Acknowledgements. This work was funded by the Marine Environmental Observation, Prediction and Response (MEOPAR) Network of Canada (grant numbers 1.2, 7.2 and 37.1). Computational resources were provided by Compute Canada for hindcast runs (grant numbers FT520, RRG2648 and RRG2969) and Ocean Networks Canada for daily nowcast runs. The SalishSeaCast software environment was developed by Doug Latornell, and the SMELT ecosystem model was developed by Elise Olson. Additionally, Vy Do performed a significant amount of the preliminary analysis leading to this study as an undergraduate co-op student. [We also thank Rich Pawlowicz at UBC for his assistance with the spectral analysis, and Jennifer Jackson at the Hakai Institute and one anonymous reviewer for their helpful comments on the manuscript.](#)

References

- Allen, S. E. and Wolfe, M. A.: Hindcast of the timing of the spring phytoplankton bloom in the Strait of Georgia, 1968–2010, *Prog. Oceanogr.*, 845 115, 6–13, <https://doi.org/10.1016/j.pocean.2013.05.026>, 2013.
- Bakri, T. and Jackson, P.: Statistical and synoptic analyses of offshore wind variations, *Int. J. Climatol.*, 39, 3201–3217, <https://doi.org/10.1002/joc.6012>, 2019.
- Bakri, T., Jackson, P., and Doherty, F.: A synoptic climatology of strong along-channel winds on the coast of British Columbia, Canada, *Int. J. Climatol.*, 37, 2398–2412, <https://doi.org/10.1002/joc.4853>, 2017a.
- 850 Bakri, T., Jackson, P., and Doherty, F.: Along-channel winds in Howe Sound: climatological analysis and case studies, *Atmos. Ocean*, 55, 12–30, <https://doi.org/10.1080/07055900.2016.1233094>, 2017b.
- Barth, J. A., Menge, B. A., Lubchenco, J., Chan, F., Bane, J. M., Kirincich, A. R., McManus, M. A., Nielsen, K. J., Pierce, S. D., and Washburn, L.: Delayed upwelling alters nearshore coastal ocean ecosystems in the northern California Current, *PNAS*, 104, 3719–3724, <https://doi.org/10.1073/pnas.0700462104>, 2007.
- 855 Bednorz, E., Pórolniczak, M., Czernecki, B., and Tomczyk, A. M.: Atmospheric forcing of coastal upwelling in the southern Baltic Sea basin, *Atmosphere*, 10, 327, <https://doi.org/10.3390/atmos10060327>, 2019.
- Bouffard, D. and Lemmin, U.: Kelvin waves in Lake Geneva, *J. Great Lakes Res.*, 39, 637–645, <https://doi.org/10.1016/j.jglr.2013.09.005>, 2013.
- Bouffard, D., Kiefer, I., Wüest, A., Wunderle, S., and Odermatt, D.: Are surface temperature and chlorophyll in a large deep lake related? An
860 analysis based on satellite observations in synergy with hydrodynamic modelling and in-situ data, *Remote Sens. Environ.*, 209, 510–523, <https://doi.org/10.1016/j.rse.2018.02.056>, 2018.
- Chan, F., Barth, J. A., Blanchette, C. A., Byrne, R. H., Chavez, F., Cheriton, O., Feely, R. A., Friederich, G., Gaylord, B., Gouhier, T., Hacker, S., T. Hill, G. H., McManus, M. A., Menge, B. A., Nielsen, K. J., Russell, A., Sanford, E., Sevadjian, J., and Washburn, L.: Persistent spatial structuring of coastal ocean acidification in the California Current System, *Nat. Sci. Rep.*, 7, 2526, <https://doi.org/10.1038/s41598-017-02777-y>, 2017.
- 865 Chavez, F. P. and Messié, M.: A comparison of Eastern Boundary Upwelling Ecosystems, *Prog. Oceanogr.*, 83, 80–96, <https://doi.org/10.1016/j.pocean.2009.07.032>, 2009.
- Choboter, P. F., Duke, D., Horton, J. P., and Sinz, P.: Exact solutions of wind-driven coastal upwelling and downwelling over sloping topography, *J. Phys. Oceanogr.*, 41, 1277–1296, <https://doi.org/10.1175/2011JPO4527.1>, 2011.
- 870 Collins, A. K., Allen, S. E., and Pawlowicz, R.: The role of wind in determining the timing of the spring bloom in the Strait of Georgia, *Can. J. Fish. Aquat. Sci.*, 66, 1597–1616, <https://doi.org/10.1139/F09-071>, 2009.
- Csanady, G. T.: Transverse internal seiches in large oblong lakes and marginal seas, *J. Phys. Oceanogr.*, 3, 439–447, [https://doi.org/10.1175/1520-0485\(1973\)003<0439:TISILO>2.0.CO;2](https://doi.org/10.1175/1520-0485(1973)003<0439:TISILO>2.0.CO;2), 1973.
- Csanady, G. T.: Barotropic currents over the continental shelf, *J. Phys. Oceanogr.*, 4, 357–371, [https://doi.org/10.1175/1520-0485\(1974\)004<0357:BCOTCS>2.0.CO;2](https://doi.org/10.1175/1520-0485(1974)004<0357:BCOTCS>2.0.CO;2), 1974.
- 875 Csanady, G. T.: Intermittent 'full' upwelling in Lake Ontario, *J. Geophys. Res.*, 82, 397–419, <https://doi.org/10.1029/JC082i003p00397>, 1977.
- Csanady, G. T.: On the structure of transient upwelling events, *J. Phys. Oceanogr.*, 12, 84–96, [https://doi.org/10.1175/1520-0485\(1982\)012<0084:OTSOTU>2.0.CO;2](https://doi.org/10.1175/1520-0485(1982)012<0084:OTSOTU>2.0.CO;2), 1982a.

- 880 Csanady, G. T.: Circulation in the Coastal Ocean, Springer, Dordrecht, Netherlands, <https://doi.org/10.1007/978-94-017-1041-1>, 1982b.
- Cushman-Roisin, B., Asplin, L., and Svendsen, H.: Upwelling in broad fjords, *Cont. Shelf Res.*, 14, 1701–1721, [https://doi.org/10.1016/0278-4343\(94\)90044-2](https://doi.org/10.1016/0278-4343(94)90044-2), 1994.
- Del Bel Belluz, J., Peña, M. A., Jackson, J. M., and Nemcek, N.: Phytoplankton composition and environmental drivers in the northern Strait of Georgia (Salish Sea), British Columbia, Canada, *Estuar. Coast.*, 44, 1419–1439, <https://doi.org/10.1007/s12237-020-00858-2>, 2021.
- 885 Delpeche-Ellmann, N., Mingelaité, T., and Soomere, T.: Examining Lagrangian surface transport during a coastal upwelling in the Gulf of Finland, Baltic Sea, *J. Mar. Sys.*, 171, 21–30, <https://doi.org/10.1016/j.jmarsys.2016.10.007>, 2017.
- Delpeche-Ellmann, N., Soomere, T., and Kudryavtseva, N.: The role of nearshore slope on cross-shore surface transport during a coastal upwelling event in Gulf of Finland, Baltic Sea, *Estuar. Coast. Shelf Sci.*, 209, 123–135, <https://doi.org/10.1016/j.ecss.2018.03.018>, 2018.
- Evans, W., Pocock, K., Hare, A., Weekes, C., Hales, B., Jackson, J., Gurney-Smith, H., Mathis, J. T., Alin, S. R., and Feely, R. A.: Marine CO₂ patterns in the northern Salish Sea, *Front. Mar. Sci.*, 5, 536, <https://doi.org/10.3389/fmars.2018.00536>, 2018.
- 890 Fatland, R., MacCready, P., and Oscar, N.: LiveOcean, in: *Cloud Computing in Ocean and Atmospheric Sciences*, edited by Vance, T. C., Merati, N., Yang, C., and Yuan, M., chap. 14, pp. 277–296, Academic Press, <https://doi.org/10.1016/B978-0-12-803192-6.00014-1>, 2016.
- Flather, R. A.: A storm surge prediction model for the northern Bay of Bengal with application to the cyclone disaster in April 1991, *J. Phys. Oceanogr.*, 24, 172–190, [https://doi.org/10.1175/1520-0485\(1994\)024<0172:ASSPMF>2.0.CO;2](https://doi.org/10.1175/1520-0485(1994)024<0172:ASSPMF>2.0.CO;2), 1994.
- 895 Foreman, M. G. G., Walters, R. A., Henry, R. F., Keller, C. P., and Dolling, A. G.: A tidal model for eastern Juan de Fuca Strait and the southern Strait of Georgia, *J. Geophys. Res. Oceans*, 100, 721–740, <https://doi.org/10.1029/94JC02721>, 1995.
- Foreman, M. G. G., Crawford, W. R., Cherniawsky, J. Y., Henry, R. F., and Tarbotton, M. R.: A high-resolution assimilating tidal model for the northeast Pacific Ocean, *J. Geophys. Res. Oceans*, 105, 28 629–28 651, <https://doi.org/10.1029/1999JC000122>, 2000.
- Haigh, R. and Taylor, F. J. R.: Mosaicism of microplankton communities in the northern Strait of Georgia, British Columbia, *Mar. Biol.*, 110, 301–314, <https://doi.org/10.1007/bf01313717>, 1991.
- 900 Hansen, P. J., Nielsen, L. T., Johnson, M., Berge, T., and Flynn, K. J.: Acquired phototrophy in *Mesodinium* and *Dinophysis* - A review of cellular organization, prey selectivity, nutrient uptake and bioenergetics, *Harmful Algae*, 28, 126–139, <https://doi.org/10.1016/j.hal.2013.06.004>, 2013.
- Harris, C. R., Millman, K. J., van der Walt, S. J., Gommers, R., Virtanen, P., Cournapeau, D., Wieser, E., Taylor, J., Berg, S., Smith, N. J., Kern, R., Picus, M., Hoyer, S., van Kerkwijk, M. H., Brett, M., Haldane, A., del Río, J. F., Wiebe, M., Peterson, P., Gérard-Marchant, P., Sheppard, K., Reddy, T., Weckesser, W., Abbasi, H., Gohlke, C., and Oliphant, T. E.: Array programming with NumPy, *Nature*, 585, 357–362, <https://doi.org/10.1038/s41586-020-2649-2>, 2020.
- 905 Hellerman, S. and Rosenstein, M.: Normal monthly wind stress over the world ocean with error estimates, *J. Phys. Oceanogr.*, 13, 1093–1104, [https://doi.org/10.1175/1520-0485\(1983\)013<1093:NMWSOT>2.0.CO;2](https://doi.org/10.1175/1520-0485(1983)013<1093:NMWSOT>2.0.CO;2), 1983.
- 910 Hollingsworth, A., Källberg, P., Renner, V., and Burridge, D. M.: An internal symmetric computational instability, *Q. J. R. Meteorolog. Soc.*, 109, 417–428, <https://doi.org/10.1002/qj.49710946012>, 1983.
- Horst, P.: *Factor Analysis of Data Matrices*, Holt, Rinehart and Winston, New York, USA, 1965.
- Hoyer, S. and Hamman, J.: xarray: N-D labeled arrays and datasets in Python, *J. Open Res. Software*, 5, <https://doi.org/10.5334/jors.148>, 2017.
- 915 Hunter, J. D.: Matplotlib: A 2D graphics environment, *Comput. Sci. Eng.*, 9, 90–95, <https://doi.org/10.1109/MCSE.2007.55>, 2007.
- Ianson, D., Allen, S. E., Moore-Maley, B. L., Johannessen, S. C., and Macdonald, R. W.: Vulnerability of a semienclosed estuarine sea to ocean acidification in contrast with hypoxia, *Geophys. Res. Lett.*, 43, 5793–5801, <https://doi.org/10.1002/2016GL068996>, 2016.

- Imam, Y. E., Laval, B., Pieters, R., and Lawrence, G.: The strongly damped baroclinic response to wind in a multibasin reservoir, *Limnol. Oceanogr.*, 58, 1243–1258, <https://doi.org/10.4319/lo.2013.58.4.1243>, 2013.
- 920 Jackson, P. L.: Surface winds during an intense outbreak of arctic air in southwestern British Columbia, *Atmos. Ocean*, 34, 285–311, <https://doi.org/10.1080/07055900.1996.9649566>, 1996.
- Johannessen, S. C., Masson, D., and Macdonald, R. W.: Oxygen in the deep Strait of Georgia, 1951–2009: the roles of mixing, deep-water renewal, and remineralization of organic carbon, *Limnol. Oceanogr.*, 59, 211–222, <https://doi.org/10.4319/lo.2014.59.1.0211>, 2014.
- Johannessen, S. C., Macdonald, R. W., and Strivens, J. E.: Has primary production declined in the Salish Sea?, *Can. J. Fish. Aquat. Sci.*, 78, 925 312–321, <https://doi.org/10.1139/cjfas-2020-0115>, 2021.
- Kämpf, J. and Chapman, P.: *Upwelling Systems of the World*, Springer, Cham, Switzerland, <https://doi.org/10.1007/978-3-319-42524-5>, 2016.
- Khangaonkar, T., Nugraha, A., Xu, W., Long, W., Bianucci, L., Ahmed, A., Mohamedali, T., and Pelletier, G.: Analysis of hypoxia and sensitivity to nutrient pollution in Salish Sea, *J. Geophys. Res. Oceans*, 123, 4735–4761, <https://doi.org/10.1029/2017JC013650>, 2018.
- 930 Kluyver, T., Ragan-Kelley, B., Pérez, F., Granger, B., Bussonnier, M., Frederic, J., Kelley, K., Hamrick, J., Grout, J., Corlay, S., Ivanov, P., Avila, D., Abdalla, S., Willing, C., and Jupyter development team: Jupyter Notebooks – a publishing format for reproducible computational workflows, in: *Positioning and Power in Academic Publishing: Players, Agents and Agendas*, edited by Loizides, F. and Schmidt, B., pp. 87–90, IOS Press, Netherlands, <https://doi.org/10.3233/978-1-61499-649-1-87>, 2016.
- Laval, B. E., Morrison, J., Potts, D. J., Carmack, E. C., Vagle, S., James, C., McLaughlin, F. A., and Foreman, M.: Wind-driven summertime 935 upwelling in a fjord-type lake and its impact on downstream river conditions: Quesnel Lake and River, British Columbia, Canada, *J. Great Lakes Res.*, 34, 189–203, [https://doi.org/10.3394/0380-1330\(2008\)34\[189:WSUIAF\]2.0.CO;2](https://doi.org/10.3394/0380-1330(2008)34[189:WSUIAF]2.0.CO;2), 2008.
- Lehmann, A., Myrberg, K., and Höfllich, K.: A statistical approach to coastal upwelling in the Baltic Sea based on the analysis of satellite data for 1990–2009, *Oceanologia*, 54, 369–393, <https://doi.org/10.5697/oc.54-3.369>, 2012.
- Lentz, S. J. and Chapman, D. C.: The importance of nonlinear cross-shelf momentum flux during wind-driven coastal upwelling, *J. Phys. Oceanogr.*, 34, 2444–2457, <https://doi.org/10.1175/JPO2644.1>, 2004.
- 940 MacCready, P., McCabe, R. M., Siedlecki, S. A., Lorenz, M., Giddings, S. N., Bos, J., Albertson, S., Banas, N. S., and Garnier, S.: Estuarine circulation, mixing, and residence times in the Salish Sea, *J. Geophys. Res. Oceans*, 126, e2020JC016738, <https://doi.org/10.1029/2020JC016738>, 2021.
- Mackas, D. L. and Harrison, P. J.: Nitrogenous nutrient sources and sinks in the Juan de Fuca Strait/Strait of Georgia/Puget Sound estuarine 945 system: assessing the potential for eutrophication, *Estuar. Coast. Shelf Sci.*, 44, 1–21, <https://doi.org/10.1006/ecss.1996.0110>, 1997.
- Madec, G., Bourdallé-Badie, R., Bouttier, P.-A., Bricaud, C., Bruciaferri, D., Calvert, D., Chanut, J., Clementi, E., Coward, A., Delrosso, D., Ethé, C., Flavoni, S., Graham, T., Harle, J., Iovino, D., Lea, D., Lévy, C., Lovato, T., Martin, N., Masson, S., Mocavero, S., Paul, J., Rousset, C., Storkey, D., Storto, A., and Vancoppenolle, M.: NEMO ocean engine, Notes du Pôle de modélisation de l’Institut Pierre-Simon Laplace (IPSL): (27), <https://doi.org/10.5281/zenodo.1472492>, revision 8625 from SVN repository, 2017.
- 950 Marchesiello, P., McWilliams, J. C., and Shchepetkin, A.: Open boundary conditions for long-term integration of regional oceanic models, *Ocean Model.*, 3, 1–20, [https://doi.org/10.1016/S1463-5003\(00\)00013-5](https://doi.org/10.1016/S1463-5003(00)00013-5), 2001.
- Masson, D.: Deep water renewal in the Strait of Georgia, *Estuar. Coast. Shelf Sci.*, 54, 115–126, <https://doi.org/10.1006/ecss.2001.0833>, 2002.
- Masson, D. and Peña, A.: Chlorophyll distribution in a temperate estuary: the Strait of Georgia and Juan de Fuca Strait, *Estuar. Coast. Shelf Sci.*, 82, 19–28, <https://doi.org/10.1016/j.ecss.2008.12.022>, 2009.
- 955

- McKinney, W.: Data structures for statistical computing in Python, in: Proceedings of the 9th Python in Science Conference, edited by van der Walt, S. and Millman, J., pp. 56–61, <https://doi.org/10.25080/Majora-92bf1922-00a>, 2010.
- Messié, M. and Chavez, F. P.: Seasonal regulation of primary production in eastern boundary upwelling systems, *Prog. Oceanogr.*, 134, 1–18, <https://doi.org/10.1016/j.pocean.2014.10.011>, 2015.
- 960 Met Office: Cartopy: a cartographic Python library with a Matplotlib interface, Exeter, Devon, <https://doi.org/10.5281/zenodo.3783894>, 2010-2015.
- Milbrandt, J. A., Bélair, S., Faucher, M., Vallée, M., Carrera, M. L., and Glazer, A.: The pan-Canadian high resolution (2.5 km) deterministic prediction system, *Weather Forecast.*, 31, 1791–1816, <https://doi.org/10.1175/WAF-D-16-0035.1>, 2016.
- Moore-Maley, B. L., Allen, S. E., and Ianson, D.: Locally driven interannual variability of near-surface pH and Ω_A in the Strait of Georgia, 965 J., *Geophys. Res. Oceans*, 121, 1600–1625, <https://doi.org/10.1002/2015JC011118>, 2016.
- Morrison, J., Foreman, M. G. G., and Masson, D.: A method for estimating monthly freshwater discharge affecting British Columbia coastal waters, *Atmos. Ocean*, 50, 1–21, <https://doi.org/10.1080/07055900.2011.637667>, 2012.
- Mysak, L. A. and Tang, C. L.: Kelvin wave propagation along an irregular coastline, *J. Fluid Mech.*, 64, 241–262, <https://doi.org/10.1017/S0022112074002382>, 1974.
- 970 Mziray, P., Kimirei, I. A., Staehr, P. A., Lugomela, C. V., Perry, W. L., Trolle, D., O'Reilly, C. M., and Mgana, H. F.: Seasonal patterns of thermal stratification and primary production in the northern parts of Lake Tanganyika, *J. Great Lakes Res.*, 44, 1209–1220, <https://doi.org/10.1016/j.jglr.2018.08.015>, 2018.
- Olson, E. M., Allen, S. E., Do, V., Dunphy, M., and Ianson, D.: Assessment of nutrient supply by a tidal jet in the northern Strait of Georgia based on a biogeochemical model, *J. Geophys. Res. Oceans*, 125, e2019JC015766, <https://doi.org/10.1029/2019JC015766>, 2020.
- 975 Overland, J. E. and Walter Jr., B. A.: Gap winds in the Strait of Juan de Fuca, *Mon. Weather Rev.*, 109, 2221–2233, [https://doi.org/10.1175/1520-0493\(1981\)109<2221:GWITSO>2.0.CO;2](https://doi.org/10.1175/1520-0493(1981)109<2221:GWITSO>2.0.CO;2), 1981.
- Parsons, T. R., Stronach, J., Borstad, G. A., Louttit, G., and Perry, R. I.: Biological fronts in the Strait of Georgia, British Columbia, and their relation to recent measurements of primary productivity, *Mar. Ecol. Prog. Ser.*, 6, 237–242, <https://doi.org/10.3354/meps006237>, 1981.
- Pawlowicz, R., Riche, O., and Halverson, M.: The circulation and residence time of the Strait of Georgia using a simple mixing-box approach, 980 *Atmos. Ocean*, 45, 173–193, <https://doi.org/10.3137/ao.450401>, 2007.
- Pawlowicz, R., Di Costanzo, R., Halverson, M., Devred, E., and Johannessen, S.: Advection, surface area, and sediment load of the Fraser River plume under variable wind and river forcing, *Atmos. Ocean*, 55, 293–313, <https://doi.org/10.1080/07055900.2017.1389689>, 2017.
- Pawlowicz, R., Hannah, C., and Rosenberger, A.: Lagrangian observations of estuarine residence times, dispersion, and trapping in the Salish Sea, *Estuar. Coast. Shelf Sci.*, 225, 106246, <https://doi.org/10.1016/j.ecss.2019.106246>, 2019.
- 985 Pawlowicz, R., Suzuki, T., Chappell, R., Ta, A., and Esenkulova, S.: Atlas of oceanographic conditions in the Strait of Georgia (2015-2019) based on the Pacific Salmon Foundation's citizen science dataset, *Can. Tech. Rep. Fish. Aquat. Sci.*, 3374, vii+116 p., 2020.
- Percival, D. B. and Walden, A. T.: Spectral Analysis for Physical Applications, Cambridge University Press, Cambridge, UK, <https://doi.org/10.1017/CBO9780511622762>, 1993.
- Plattner, S., Mason, D. M., Leshkevich, G. A., Schwab, D. J., and Rutherford, E. S.: Classifying and forecasting coastal upwellings in 990 Lake Michigan using satellite derived temperature images and buoy data, *J. Great Lakes Res.*, 32, 63–76, [https://doi.org/10.3394/0380-1330\(2006\)32\[63:CAFUI\]2.0.CO;2](https://doi.org/10.3394/0380-1330(2006)32[63:CAFUI]2.0.CO;2), 2006.
- Preisendorfer, R. W.: Principal Component Analysis in Meteorology and Oceanography, Elsevier, Amsterdam, Netherlands, 1988.

- Roberts, D. C., Egan, G. C., Forrest, A. L., Largier, J. L., Bombardelli, F. A., Laval, B. E., Monismith, S. G., and Schladow, G.: The setup and relaxation of spring upwelling in a deep, rotationally influenced lake, *Limnol. Oceanogr.*, <https://doi.org/10.1002/lno.11673>, 2021.
- 995 Roubeyrie, L. and Celles, S.: Windrose: A Python Matplotlib, NumPy library to manage wind and pollution data, draw windrose, *J. Open Source Softw.*, 3, 268, <https://doi.org/10.21105/joss.00268>, 2018.
- Rowe, M. D., Anderson, E. J., Beletsky, D., Stow, C. A., Moegling, S. D., Chaffin, J. D., May, J. C., Collingsworth, P. D., Jabbari, A., and Ackerman, J. D.: Coastal upwelling influences hypoxia spatial patterns and nearshore dynamics in Lake Erie, *J. Geophys. Res. Oceans*, 124, 6154–6175, <https://doi.org/10.1029/2019JC015192>, 2019.
- 1000 Salvatier, J., Wiecki, T. V., and Fonnesbeck, C.: Probabilistic programming in Python using PyMC3, *PeerJ Comput. Sci.*, 2, e55, <https://doi.org/10.7717/peerj-cs.55>, 2016.
- Shintani, T., de la Fuente, A., Niño, Y., and Imberger, J.: Generalizations of the Wedderburn number: Parameterizing upwelling in stratified lakes, *Limnol. Oceanogr.*, 55, 1377–1389, <https://doi.org/10.4319/lo.2010.55.3.1377>, 2010.
- Silvestrova, K., Myslenkov, S., and Zatsepin, A.: Variability of wind-driven coastal upwelling in the north-eastern Black Sea in 1979–2016 according to NCEP/CFSR data, in: *Meteorology and Climatology of the Mediterranean and Black Seas*, edited by Vilibić, I., Horvath, K., and Palau, J. L., *Pageoph Topical Volumes*, pp. 287–295, Birkhäuser, Cham, https://doi.org/10.1007/978-3-030-11958-4_17, 2019.
- 1005 Soontiens, N. and Allen, S. E.: Modelling sensitivities to mixing and advection in a sill-basin estuarine system, *Ocean Model.*, 112, 17–32, <https://doi.org/10.1016/j.ocemod.2017.02.008>, 2017.
- Soontiens, N., Allen, S. E., Latornell, D., Souëf, K. L., Machuca, I., Paquin, J.-P., Lu, Y., Thompson, K., and Korabel, V.: Storm surges in the Strait of Georgia simulated with a regional model, *Atmos. Ocean*, 54, 121, <https://doi.org/10.1080/07055900.2015.1108899>, 2016.
- 1010 Stahl, K., Moore, R. D., and Mckendry, I. G.: The role of synoptic-scale circulation in the linkage between large-scale ocean–atmosphere indices and winter surface climate in British Columbia, Canada, *Int. J. Climatol.*, 26, 541–560, <https://doi.org/10.1002/joc.1268>, 2006.
- Stevens, C. L. and Imberger, J.: The initial response of a stratified lake to a surface shear stress, *J. Fluid Mech.*, 312, 39–66, <https://doi.org/10.1017/S0022112096001917>, 1996.
- 1015 Stevens, C. L. and Lawrence, G. A.: Estimation of wind-forced internal seiche amplitudes in lakes and reservoirs, with data from British Columbia, Canada, *Aquat. Sci.*, 59, 115–134, <https://doi.org/10.1007/BF02523176>, 1997.
- Suchy, K. D., Le Baron, N., Hilborn, A., Perry, R. I., and Costa, M.: Influence of environmental drivers on spatio-temporal dynamics of satellite-derived chlorophyll *a* in the Strait of Georgia, *Prog. Oceanogr.*, 176, 102–134, <https://doi.org/10.1016/j.pocean.2019.102134>, 2019.
- 1020 Sutton, J. N., Johannessen, S. C., and Macdonald, R. W.: A nitrogen budget for the Strait of Georgia, British Columbia, with emphasis on particulate nitrogen and dissolved inorganic nitrogen, *Biogeosci.*, 10, 7179–7194, <https://doi.org/10.5194/bg-10-7179-2013>, 2013.
- Thomson, R. E. and Huggett, W. S.: M2 baroclinic tides in Johnstone Strait, British Columbia, *J. Phys. Oceanogr.*, 10, 1509–1539, [https://doi.org/10.1175/1520-0485\(1980\)010<1509:MBTIJS>2.0.CO;2](https://doi.org/10.1175/1520-0485(1980)010<1509:MBTIJS>2.0.CO;2), 1980.
- Thomson, R. E., Beamish, R. J., Beacham, T. D., Trudel, M., Whitfield, P. H., and Hourston, R. A. S.: Anomalous ocean conditions may explain the recent extreme variability in Fraser River sockeye salmon production, *Mar. Coast. Fish.*, 4, 415–437, <https://doi.org/10.1080/19425120.2012.675985>, 2012.
- 1025 Thomson, R. E., Kulikov, E. A., Spear, D. J., Johannessen, S. C., and Wills, W. P.: A role for gravity currents in cross-sill estuarine exchange and subsurface inflow to the southern Strait of Georgia, *J. Geophys. Res. Oceans*, 125, e2019JC015374, <https://doi.org/10.1029/2019JC015374>, 2020.

- 1030 Unidata: Network Common Data Form (netCDF) version 4.5.4 [software], UCAR/Unidata, Boulder, CO, <https://doi.org/10.5065/D6H70CW6>, 2019.
- Valerio, G., Pilotti, M., Marti, C. L., and Imberger, J.: The structure of basin-scale internal waves in a stratified lake in response to lake bathymetry and wind spatial and temporal distribution: Lake Iseo, Italy, *Limnol. Oceanogr.*, *57*, 772–786, <https://doi.org/10.4319/lo.2012.57.3.0772>, 2012.
- 1035 Virtanen, P., Gommers, R., Oliphant, T. E., Haberland, M., Reddy, T., Cournapeau, D., Burovski, E., Peterson, P., Weckesser, W., Bright, J., van der Walt, S. J., Brett, M., Wilson, J., Millman, K. J., Mayorov, N., Nelson, A. R. J., Jones, E., Kern, R., Larson, E., Carey, C. J., Polat, İ., Feng, Y., Moore, E. W., VanderPlas, J., Laxalde, D., Perktold, J., Cimrman, R., Henriksen, I., Quintero, E. A., Harris, C. R., Archibald, A. M., Ribeiro, A. H., Pedregosa, F., van Mulbregt, P., and SciPy 1.0 Contributors: SciPy 1.0: fundamental algorithms for scientific computing in Python, *Nat. Methods*, *17*, 261–272, <https://doi.org/10.1038/s41592-019-0686-2>, 2020.
- 1040 Wasmund, N., Nausch, G., and Voss, M.: Upwelling events may cause cyanobacteria blooms in the Baltic Sea, *J. Mar. Sys.*, *90*, 67–76, <https://doi.org/10.1016/j.jmarsys.2011.09.001>, 2012.
- Wasser, S. K., Lundin, J. I., Ayres, K., Seely, E., Giles, D., Balcomb, K., Hempelmann, J., Parsons, K., and Booth, R.: Population growth is limited by nutritional impacts on pregnancy success in endangered Southern Resident killer whales (*Orcinus orca*), *PLoS One*, *12*, e0179824, <https://doi.org/10.1371/journal.pone.0179824>, 2017.
- 1045 Wessel, P. and Smith, W. H. F.: A global, self-consistent, hierarchical, high-resolution shoreline database, *J. Geophys. Res. Solid Earth*, *101*, 8741–8743, <https://doi.org/10.1029/96JB00104>, 1996.
- Westra, S., Brown, C., Lall, U., Koch, I., and Sharma, A.: Interpreting variability in global SST data using independent component analysis and principal component analysis, *Int. J. Climatol.*, *30*, 333–346, <https://doi.org/10.1002/joc.1888>, 2010.
- Yin, K., Goldblatt, R. H., Harrison, P. J., John, M. A. S., Clifford, P. J., and Beamish, R. J.: Importance of wind and river discharge in influencing nutrient dynamics and phytoplankton production in summer in the central Strait of Georgia, *Mar. Ecol. Prog. Ser.*, *161*, 173–183, <https://doi.org/10.3354/meps161173>, 1997.
- 1050 Zhurbas, V., Laanemets, J., and Vahtera, E.: Modeling of the mesoscale structure of coupled upwelling/downwelling events and the related input of nutrients to the upper mixed layer in the Gulf of Finland, Baltic Sea, *J. Geophys. Res. Oceans*, *133*, C05004, <https://doi.org/10.1029/2007JC004280>, 2008.